Causal links between Arctic sea ice and its potential drivers based on the rate of information transfer

David Docquier[1], Stephane Vannitsem[1], Francesco Ragone[2], Klaus Wyser[3], and X. San Liang[4]

[1]Royal Meteorological Institute of Belgium
[2]Royal Meteorological Institute of Belgium and Université Catholique de Louvain
[3]SMHI
[4]Nanjing University of Information Science and Technology, Nanjing, China

November 24, 2022

Abstract

Arctic sea ice has substantially changed over the past four decades, with a large decrease in sea-ice area and volume. The exact causes of these changes are not entirely known. In our study, we make use of the Swedish Meteorological and Hydrological Institute Large Ensemble (SMHI-LENS). This ensemble consists of 50 members realized with the EC-Earth3 global climate model and covers the period 1970-2100. We apply the Liang-Kleeman information flow method to analyze the cause-effect relationships between Arctic sea ice and its potential drivers. We show that recent and future changes in Arctic sea ice are mainly driven by air and sea-surface temperatures and ocean heat transport. Conversely, changes in Arctic sea ice also considerably impact temperature and ocean heat transport. Finally, we find a progressive decrease in the influence of sea-ice area and volume on air temperature and ocean heat transport through the twenty-first century.

Causal links between Arctic sea ice and its potential drivers based on the rate of information transfer

D. Docquier[1], S. Vannitsem[1], F. Ragone[1,2], K. Wyser[3], X. S. Liang[4]

[1]Royal Meteorological Institute of Belgium, Brussels, Belgium
[2]Université catholique de Louvain, Louvain-la-Neuve, Belgium
[3]Rossby Centre, Swedish Meteorological and Hydrological Institute, Norrköping, Sweden
[4]Fudan University, Shanghai, China

Key Points:

- The Liang-Kleeman rate of information transfer allows to quantify the directional dependence between Arctic sea ice and its drivers
- Recent and future changes in Arctic sea ice are mainly driven by air and sea-surface temperatures and ocean heat transport
- The influence of Arctic sea ice on air temperature and ocean heat transport progressively decreases through the twenty-first century

Corresponding author: David Docquier, `david.docquier@meteo.be`

Abstract

Arctic sea ice has substantially changed over the past four decades, with a large decrease in sea-ice area and volume. The exact causes of these changes are not entirely known. In our study, we make use of the Swedish Meteorological and Hydrological Institute Large Ensemble (SMHI-LENS). This ensemble consists of 50 members realized with the EC-Earth3 global climate model and covers the period 1970-2100. We apply the Liang-Kleeman information flow method to analyze the cause-effect relationships between Arctic sea ice and its potential drivers. We show that recent and future changes in Arctic sea ice are mainly driven by air and sea-surface temperatures and ocean heat transport. Conversely, changes in Arctic sea ice also considerably impact temperature and ocean heat transport. Finally, we find a progressive decrease in the influence of sea-ice area and volume on air temperature and ocean heat transport through the twenty-first century.

Plain Language Summary

The Arctic has been warming at a larger rate than the rest of the world, resulting in a substantial loss of sea ice since the late 1970s. This has had and will continue to have an impact on our climate and societies. The exact causes of the ongoing sea-ice loss are not entirely known, and understanding them is important in order to better prepare our societies to future climate changes. In our study, we apply a relatively novel approach that quantifies the cause-effect relationships between Arctic sea ice and its potential drivers. We make use of a large range of model simulations performed with the EC-Earth3 global climate model covering the period 1970-2100. We find that air temperature, sea-surface temperature and the transport of heat by the ocean are important drivers of the ongoing and future retreat of Arctic sea ice. Conversely, changes in Arctic sea ice also affect the three former quantities. Our study demonstrates the performance of causal inference methods in the quest of better understanding relationships between climate variables. The geophysical and climate communities could greatly benefit from using these methods more intensively.

1 Introduction

Arctic sea ice has been retreating and thinning since the beginning of satellite observations in the late 1970s. Arctic sea-ice area, defined as the total area of the Arctic Ocean covered by sea ice, has decreased by ~ 2 million km^2 (in annual mean) since 1979, with stronger loss in summer compared to winter (Onarheim et al., 2018; Stroeve & Notz, 2018; IPCC, 2019). As sea ice has also been thinning (Lindsay & Schweiger, 2015; Kwok, 2018), the annnual mean Arctic sea-ice volume has decreased by $\sim 12{,}000$ km^3 since 1979 (Schweiger et al., 2019). Model projections show a more or less rapid continuation of this ongoing process depending on the greenhouse gas emission scenario, with likely summer ice-free Arctic conditions (September Arctic sea-ice area lower than 1 million km^2) occurring before 2050 (SIMIP Community, 2020; Arthun et al., 2021; Docquier & Koenigk, 2021).

Recent changes in Arctic sea ice have been linked to both anthropogenic global warming (Notz & Stroeve, 2016) and climate internal variability (Swart et al., 2015). However, the exact drivers influencing sea-ice loss and their respective contribution are not fully understood. Both atmospheric (Ding et al., 2017) and ocean (Carmack et al., 2015) processes play a role in Arctic sea-ice changes. Typically, changes in near-surface air temperature strongly control the variability in Arctic sea-ice area over short time scales (Olonscheck et al., 2019), while ocean heat transport has a stronger impact on longer time scales (Onarheim et al., 2015).

The influence of atmospheric and ocean processes on Arctic sea ice is usually quantified via correlation and regression analyses, including or not a lag (Arthun et al., 2012;

Sando et al., 2014; Auclair & Tremblay, 2018). However, the presence of a correlation between one variable and another does not firmly demonstrate a causal influence between these variables. In order to identify such a causal link, causal inference frameworks can be used (Granger, 1969; Sugihara et al., 2012; Liang, 2014; Krakovska et al., 2018; Runge et al., 2019) and have been applied to climate studies (e.g. Mosedale et al. (2006); Deza et al. (2015); Tsonis et al. (2015); Kretschmer et al. (2016); Vannitsem and Ekelmans (2018); Harries and O'Kane (2021)). The Liang-Kleeman information flow method (Liang & Kleeman, 2005) is particularly interesting because it allows to identify the direction and magnitude of the cause-effect relationships between variables (Liang, 2014, 2021). This novel method has been successfully applied to several climate studies (Stips et al., 2016; Vannitsem et al., 2019) and constitutes an adequate framework to identify causal relationships between different climate variables.

In our study, we use the Liang-Kleeman information flow method to analyze the influence of several potential climate drivers on Arctic sea-ice area and volume, as well as the reverse impact of sea-ice area and volume on these drivers. We make use of the Swedish Meteorological and Hydrological Institute Large Ensemble (SMHI-LENS) to perform this analysis. We describe the data and methodology in Section 2, present our main results in Section 3, and provide our conclusions in Section 4.

2 Data and Methods

SMHI-LENS is one of the largest existing single-model large ensembles using the Coupled Model Intercomparison Project 6 (CMIP6; Eyring et al. (2016)) forcing scenarios. It consists of 50 members realized with the global climate model EC-Earth3 (Wyser et al., 2021). The atmosphere component, IFS cy36r4, has a horizontal resolution of ~ 80 km, while the ocean component, NEMO3.6 (including the sea-ice model LIM3), has a horizontal resolution of $\sim 1^\circ$. The 50 ensemble members were started in 1970 from 50 different initial conditions using CMIP6 historical forcing and run until 2014. From 2015 until the end of the century, each member was run several times to take into account different greenhouse gas emission scenarios based on the Shared Socioeconomic Pathways (SSP; O'Neill et al. (2016)). More details about the SMHI-LENS protocol can be found in Wyser et al. (2021). In our study, we use the 50 members of SMHI-LENS over the historical period (1970-2014) and over the two most extreme SSP scenarios (2015-2100), i.e. SSP1-1.9 and SSP5-8.5, corresponding to an increase in global mean near-surface temperature of less than 2°C and $\sim 6^\circ$C, respectively, between 1970 and 2100 (Wyser et al., 2021).

From the model outputs, we compute Arctic sea-ice area (volume) based on the product of sea-ice concentration (sea-ice volume per area, respectively) in each grid point and grid-cell area, summed over all grid points north of 40°N. We focus on sea-ice area and volume in March and September, as these are months of maximum and minimum sea-ice area, respectively. We also compute six quantities that constitute potential atmospheric and ocean drivers of changes in Arctic sea ice: Arctic near-surface air temperature, Arctic sea-surface temperature (SST), total Arctic Ocean heat transport, ocean heat transport at 70°N, atmospheric heat transport at 70°N, and Arctic Oscillation Index (AOI). We take the annual mean for the first five quantities, and the winter (January-March) average for AOI. Arctic near-surface and sea-surface temperatures are spatially averaged north of 70°N. Total Arctic Ocean heat transport is the sum of ocean heat transport through the four main Arctic gates (Barents Sea Opening, Fram Strait, Davis Strait, Bering Strait), which are computed via the product of ocean temperature and velocity integrated across depth and the corresponding transects, as in Docquier et al. (2021). Ocean and atmospheric heat transports at 70°N are estimated based on the net downward surface heat flux and top-of-the atmosphere radiation, as in van der Linden et al. (2019). AOI is computed based on monthly mean 1000 hPa geopotential height anomalies from 20°N to 90°N, as in Zhang et al. (2021).

In the high-emission scenario (SSP5-8.5), the ensemble mean March sea-ice area and volume decrease by 62 % and 94 %, respectively, across the 131 years of model simulation and the September sea ice completely disappears around 2060 (Figure 1a,b). This sea-ice loss is associated with an increase in Arctic near-surface temperature and SST of 18°C and 7°C, respectively (Figure 1c), an enhanced total Arctic Ocean heat transport of 180 TW (Figure 1d), and an increase in ocean heat transport at 70°N of 1.2 PW (Figure 1e) at the end of the century compared to 1970. The atmospheric heat transport at 70°N slightly decreases (-0.3 PW) across the twenty-first century (Figure 1e), and no significant change is detected for AOI due to large interannual variability (Figure 1f). In the low-emission scenario (SSP1-1.9), these changes are also apparent but with a much lower magnitude and a stabilization around the middle of the century (Figure S1). Especially, Arctic sea ice is still present in September and the ensemble mean September sea-ice area stabilizes at 1.8 million km^2 from around 2040 to 2100. Note that ocean heat transport at 70°N in SSP1-1.9 first increases until around 2030 and then decreases to its 1970 values. In our study, we focus on SSP5-8.5 as the results between the two scenarios are relatively consistent in terms of transfer of information, but we also discuss differences between scenarios if they exist.

The absolute rate of information transfer from variable X_j to variable X_i is computed following Liang (2021):

$$T_{j\to i} = \frac{1}{\det\mathbf{C}} \cdot \sum_{k=1}^{d} \Delta_{jk} C_{k,di} \cdot \frac{C_{ij}}{C_{ii}}, \tag{1}$$

where $\mathbf{C}$ is the covariance matrix, d is the number of variables ($d = 7$ in our case), Δ_{ij} are the cofactors of $\mathbf{C}$, $C_{k,di}$ is the sample covariance between all X_k and the Euler forward difference approximation of dX_i/dt (t is time), C_{ij} is the sample covariance between X_i and X_j, C_{ii} is the sample variance of X_i. When $T_{j\to i}$ is statistically different from 0, X_j has an influence on X_i, while if $T_{j\to i} = 0$ there is no influence. Statistical significance is computed via bootstrap resampling with replacement of all terms included in equation (1) using 1000 realizations.

To assess the importance of the different cause-effect relationships, we compute the relative rate of information transfer from variable X_j to variable X_i following Liang (2021):

$$\tau_{j\to i} = \frac{T_{j\to i}}{Z}, \tag{2}$$

where Z is the normalizer, computed as follows:

$$Z = \left|\frac{dH_i^*}{dt}\right| + \sum_{k=2}^{d} |T_{k\to i}| + \left|\frac{dH_i^{noise}}{dt}\right|, \tag{3}$$

where the first term on the right-hand side is the influence of X_i on itself (self-influence), the second term represents the information flowing from all the X_k to X_i, and the last term is the effect of noise, computed following Liang (2021). When $|\tau| = 100$ %, X_j has the maximum influence on X_i, while when $|\tau| = 0$ %, X_j has no influence on X_i. As for $T_{j\to i}$, statistical significance of $\tau_{j\to i}$ is computed via bootstrap resampling with replacement of all terms included in equations (2) and (3) using 1000 realizations. For both $T_{j\to i}$ and $\tau_{j\to i}$, the 95% confidence interval is built based on the standard deviation of bootstrapped absolute and relative rates of information transfer, respectively, multiplied by 1.96.

We compute the transfer of information including the seven variables described above, where sea ice is either March sea-ice area, September sea-ice area, March sea-ice volume or September sea-ice volume. This allows to check the role of sea-ice seasonality and the effect of using sea-ice thickness information or not. Two different methods for computing the rate of information transfer are used. In the first method, hereafter referred to

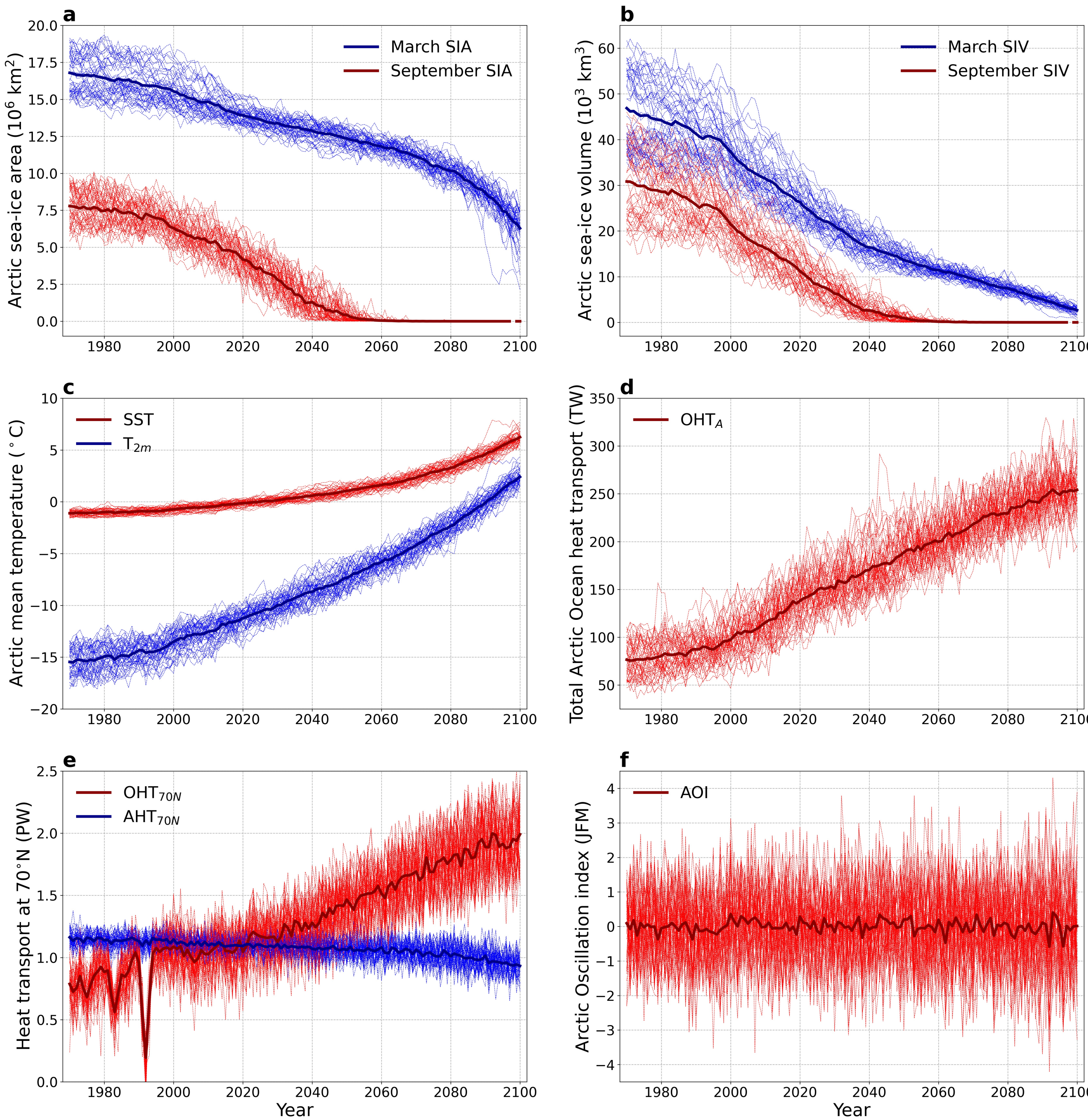

Figure 1. Time series of all considered variables for the 50 EC-Earth3 members (thin lines) and the ensemble mean (dark thick lines) over 1970-2100 (historical CMIP6 run and SSP5-8.5 scenario). (a) March and September Arctic sea-ice area (SIA); (b) March and September Arctic sea-ice volume (SIV); (c) annual mean Arctic near-surface temperature (T_{2m}) and Arctic sea-surface temperature (SST); (d) annual mean total Arctic Ocean heat transport (OHT_A); (e) annual mean poleward ocean and atmospheric heat transports at 70°N (OHT_{70N} and AHT_{70N}); (f) winter (JFM) Arctic Oscillation index (AOI).

as 'member analysis', the rate of information transfer is computed for each member separately. As the information flow method applies to stationary time series (see Supporting Information), we detrend each quantity before computing the rate of information transfer by removing the ensemble mean for each model member (Figure S2). Due to the limited amount of September sea ice after 2040 and as the two last decades show a strong acceleration in the reduction of March sea-ice area in the high-emission scenario (Figure 1a), we limit our analysis to 1970-2040 for September (71 data points for each member) and 1970-2080 for March (111 data points for each member). We take the ensemble mean rate of information transfer and check the statistical significance via the Fisher's method for multiple tests (Fisher (1992); Figure 2). In the second method, hereafter referred to as 'time analysis', the rate of information transfer is computed for each range of five years separately (across the member space, resulting in 250 data points for each period of five years, except for the last period 2095-2100 including six years). The latter method allows to check the time evolution of the rate of information transfer between variables (Figures 3-4). Having 50 ensemble members allows to reduce the uncertainty related to internal variability (Jahn et al., 2016) for the member analysis, and brings a sufficient number of data points for the time analysis.

3 Results

3.1 Member Analysis

Figure 2 provides a summary of results from the member analysis as matrices of ensemble mean relative rate of information transfer and correlation coefficient between March / September sea-ice area and its potential drivers based on SSP5-8.5. The self-influence of variables (shown in the matrix diagonals) is the largest compared to other influences ($|\tau|$ ranging between 38 and 69 %), indicating a strong feedback loop (Figure 2a,c).

Beside these self-influences, there is a two-way significant information transfer between March sea-ice area on the one hand, and Arctic SST and Arctic Ocean heat transport on the other hand, as well as a significant influence of March sea-ice area on near-surface temperature (Figure 2a). These causal links are stronger from March sea-ice area to near-surface temperature ($|\tau| = 15$ %), to SST ($|\tau| = 11$ %), and to Arctic Ocean heat transport ($|\tau| = 11$ %; first row in Figure 2a), than the reverse (first column in Figure 2a). This suggests that recent and future changes in March sea-ice area have a strong impact on Arctic temperatures (both at the sea surface and air surface) and ocean heat transport, probably via the ice-albedo feedback (Andry et al., 2017; Massonnet et al., 2018; Wunderling et al., 2020). Additionally, correlation coefficients are negative between March sea-ice area and Arctic near-surface temperature (R = -0.79), Arctic SST (R = -0.75), and Arctic Ocean heat transport (R = -0.59; Figure 2b). Thus, combining the relative rates of information transfer and correlation coefficients, we can infer that the ongoing decrease in March sea-ice area leads to larger SST, larger near-surface temperature and larger ocean heat transport in the Arctic. Although slightly weaker, a similar conclusion can be drawn for the influence of SST and ocean heat transport on March sea-ice area.

By contrast with March, September sea-ice area has a significant influence only on near-surface temperature (but this is relatively reduced, i.e. $|\tau| = 5$ %; Figure 2c). Also, while changes in March sea-ice area are mainly driven by changes in SST ($|\tau| = 9$ %) and Arctic Ocean heat transport ($|\tau| = 8$ %; Figure 2a), changes in September sea-ice area primarily come from changes in near-surface temperature ($|\tau| = 13$ %; Figure 2c). Arctic sea-ice area is more than twice larger in March compared to September (Figure 1a), and sea ice is present in March in (or close to) regions where large increases in ocean heat transport and SST have been reported in the past years, such as the Barents Sea (Arthun et al., 2012), Laptev Sea (Polyakov et al., 2017), and Chukchi Sea (Serreze et al., 2019). Thus, the role of a warming ocean and enhanced ocean heat transport on sea ice is greater in March compared to September. As sea ice is much more confined to the central Arctic in September, the primary driver of September sea-ice area decrease in the past years is the air temperature. Thus, these results support a winter ocean-driven influence and a summer atmospheric-led influence.

Results from the member analysis are relatively similar for the weak greenhouse gas emission scenario (SSP1-1.9), with a larger influence of March sea-ice area on Arctic near-surface temperature and ocean heat transport than the reverse, a larger impact of the atmosphere (near-surface temperature) on sea-ice area in September than in March, and a stronger causal link from the ocean (SST) to sea-ice area in March (Figure S3). An exception in SSP1-1.9, compared to SSP5-8.5, is that there is no significant information transfer from ocean heat transport to March and September sea-ice area. When taking sea-ice volume instead of sea-ice area, the influence of near-surface temperature and SST on March sea-ice volume becomes larger than the reverse in the two emission scenarios (Figures S4a and S5a). This suggests that temperature changes at the surface of the ocean and above greatly affect sea-ice thickness. In September, near-surface temperature constitutes the largest driver of sea-ice volume, similar to sea-ice area, but during this month sea-ice volume also affects SST and Arctic Ocean heat transport (Figures S4c and S5c), while it is not the case for sea-ice area (Figures 2c and S3c). Thus, changes in sea-ice thickness play an important role in driving changes in ocean temperature and heat transport.

For the two scenarios, no causal influence is detected between sea-ice area and volume in March and September on the one hand, and ocean and atmospheric heat transports at 70°N and AOI on the other hand. Interestingly, a significantly positive correlation appears between March sea-ice area and atmospheric heat transport at 70°N ($R = 0.23$; Figure 2b), but no transfer of information exists (Figure 2a). This suggests that an external driver causes concomitant changes in sea-ice area and atmospheric heat transport, while these two quantities do not influence each other. The main suspect is SST as it influences both variables: an increase in SST leads to lower sea-ice area and lower atmospheric heat transport at 70°N (Figure 2a,b). This further demonstrates that correlation does not mean causation and shows the strength of the Liang-Kleeman information flow method (Liang, 2014). For ocean heat transport at 70°N, the absence of correlation and causal link with sea ice indicates an absence of connection at such latitude, as is the case for other climate models (Burgard & Notz, 2017; Docquier et al., 2019).

3.2 Time Analysis

Based on the previous member analysis (Section 3.1), near-surface temperature, SST and Arctic Ocean heat transport have an influence on Arctic sea ice, and conversely. For the time analysis, we focus on the cause-effect relationships between near-surface air temperature and Arctic Ocean heat transport on the one hand, and Arctic sea-ice area and volume on the other hand. We do not consider SST as this quantity is somewhat integrated into ocean heat transport and is thus redundant.

The correlation coefficient between March Arctic sea-ice area and Arctic near-surface temperature stays relatively constant through the whole time period with large negative values (R = -0.75 to -0.9; Figure 3a), in agreement with previous studies (e.g. Olonscheck et al. (2019)). The relative rate of information transfer from near-surface temperature to March sea-ice area shows a large five-year variability, with a peak in 1975-1979 ($|\tau| \approx$ 25 %) and four additional five-year periods having a significant influence (Figure 3a). The number of periods with a significant rate of information transfer from March sea-ice area to near-surface temperature is twice more important (i.e. 11 periods) than the reverse influence (Figure 3a), which confirms previous results from the member analysis (Section 3.1). Additionally, no significant influence of March sea-ice area on near-surface temperature remains after 2050, while one five-year period shows an influence of temperature on sea-ice area after 2050 (Figure 3a). In September, the rate of information transfer from near-surface temperature to sea-ice area is generally larger than from sea-ice area to temperature, and peaks in 2025-2029 before decreasing (Figure S6a).

As for the information transfer from March sea-ice area to near-surface temperature, the rate of information transfer from March sea-ice area to Arctic Ocean heat transport generally decreases over time, with no significant influence after 2050 (Figure 3b). For the reverse transfer of information from ocean heat transport to Arctic sea-ice area, eight periods are significant, with four periods after 2050, but with relatively low values ($|\tau|$ = 6-7 %). Year 2050 also marks a threshold after which the correlation coefficient between March sea-ice area and ocean heat transport starts decreasing from $R \approx$ -0.7 on average for 1970-2049 to $R =$ -0.25 in 2095-2100 (Figure 3b). Thus, as sea-ice area becomes smaller, the two-way influence between sea-ice area and near-surface temperature and ocean heat transport becomes weaker. This is also the case in September with a decrease starting earlier on due to lower sea-ice area during that month (Figure S6b). Results are qualitatively similar in the low greenhouse gas emission scenario (Figures S7-S8).

Contrarily to the rate of information transfer from near-surface temperature to March sea-ice area, the information transfer from near-surface temperature to March sea-ice volume remains strong almost until the end of the century, with values of $|\tau|$ between $\sim$ 15 and 35 % (Figure 4a). This means that the increase in air temperature leads to a decrease in sea-ice volume until the end of the century. Changes in March sea-ice volume also influence changes in near-surface temperature, but with lower values of information transfer than the reverse influence and a progressive decrease across time (Figure 4a). In September, the information transfer is also generally larger from near-surface temperature to sea-ice volume than the reverse, except in the beginning of the model simulation (1970-1999; Figure S9a).

As for the March sea-ice area - ocean heat transport relationship, the correlation coefficient between March sea-ice volume and ocean heat transport decreases over time (Figure 4b). This coincides with a decrease over time in the influence of March sea-ice volume on ocean heat transport. The transfer of information from ocean heat transport to March sea-ice volume stays relatively low through the whole twenty-first century, with only three five-year periods showing a significant transfer of information (Figure 4b). Results are qualitatively similar when considering September sea-ice volume (Figure S9b), as well as SSP1-1.9 scenario (Figures S10-S11).

4 Conclusions and Perspectives

In our study, we have applied the Liang-Kleeman information flow method to the analysis of causal influences between Arctic sea-ice area and volume and their potential drivers using SMHI-LENS (50 members simulated with EC-Earth3). We found that the recent and future changes in Arctic sea-ice area and volume are mainly driven by near-surface air temperature, sea-surface temperature and ocean heat transport, in agreement with previous studies (Onarheim et al., 2015; Olonscheck et al., 2019). Our results support a winter-driven ocean influence on sea ice and a summer atmospheric-led influence. More surprisingly, the reverse influence of sea-ice area and volume on temperature and ocean heat transport also exists, and is sometimes larger than the reverse influence depending on the quantity (sea-ice area or volume) and the month of the year (March or September). This two-way influence indicates that the current decrease in Arctic sea-ice area and volume is not solely related to air temperature and, consequently to greenhouse gas emissions (Notz & Stroeve, 2016), but is also highly driven by feedback mechanisms between sea ice, the atmosphere and the ocean (Pithan & Mauritsen, 2014; Goosse et al., 2018).

Our results also show a progressive loss of influence of sea-ice area and volume on air temperature and ocean heat transport through the twenty-first century on the one hand. This indicates that interactions between sea ice, the atmosphere and the ocean, especially the ice-albedo feedback (Wunderling et al., 2020), become weaker as sea-ice area decreases. On the other hand, the rate of information transfer from air temperature to September Arctic sea-ice area and volume (in both March and September) remains more constant through time and relatively large. This suggests that changes in near-surface temperature have a long-lasting effect on September sea-ice area and March and September sea-ice volume. Identifying the dynamical mechanisms causing these differences in directional dependence across time should be addressed in the future. This could be achieved via an analysis of the exact processes by which sea ice melts and refreezes, combined with the Liang-Kleeman information flow method.

Acknowledgments

Model data from EC-Earth3 SMHI-LENS (Wyser et al., 2021) are available on the Earth System Grid Federation (ESGF) nodes (`https://esgf-node.llnl.gov/search/cmip6`) via a search for 'Source ID' = EC-Earth3 and 'Variant Label' = r101i1p1f1 to r150i1p1f1. The SMHI-LENS simulations were enabled by resources provided by the Swedish National Infrastructure for Computing (SNIC). The Python scripts to produce the figures of this article are available on Zenodo: `https://zenodo.org/record/5255648`. D.D. and S.V. acknowledge partial support from ROADMAP (Role of ocean dynamics and Ocean-Atmosphere interactions in Driving cliMAte variations and future Projections of impact-relevant extreme events; `http://www.jpi-climate.eu/joint-activities/joint-calls/CPILoud/ROADMAP`), a coordinated JPI-Climate/JPI-Oceans project, financed by the Belgian Federal Science Policy Office under contract B2/20E/P1/ROADMAP.

References

Andry, O., Bintanja, R., & Hazeleger, W. (2017). Time-dependent variations in the Arctic's surface albedo feedback and the link to seasonality in sea ice. *Journal of Climate*, *30*(1), 393-410. doi: 10.1175/JCLI-D-15-0849.1

Arthun, M., Eldevik, T., Smedsrud, L. H., Skagseth, O., & Ingvaldsen, R. B. (2012). Quantifying the influence of Atlantic heat on Barents Sea ice variability and retreat. *Journal of Climate*, *25*(12), 4736-4743. doi: 10.1175/JCLI-D-11-00466.1

Arthun, M., Onarheim, I. H., Dorr, J., & Eldevik, T. (2021). The seasonal and regional transition to an ice-free Arctic. *Geophysical Research Letters*, *48*(1), e2020GL090825. doi: 10.1029/2020GL090825

Auclair, G., & Tremblay, B. (2018). The role of ocean heat transport in rapid sea ice declines in the Community Earth System Model Large Ensemble. *Journal of Geophysical Research*, *123*, 8941-8957. doi: 10.1029/2018JC014525

Burgard, C., & Notz, D. (2017). Drivers of Arctic Ocean warming in CMIP5 models. *Geophysical Research Letters*, *44*, 4263-4271. doi: 10.1002/2016GL072342

Carmack, E., Polyakov, I., Padman, L., Fer, I., Hunke, E., Hutchings, J., ... Winsor, P. (2015). Toward quantifying the increasing role of oceanic heat in sea ice loss in the new Arctic. *Bulletin of the American Meteorological Society*, *96*(12), 2079-2105. doi: 10.1175/BAMS-D-13-00177.1

Deza, J., Barreiro, M., & Masoller, C. (2015). Assessing the direction of climate interactions by means of complex networks and information theoretic tools. *Chaos*, *25*, 033105. doi: 10.1063/1.4914101

Ding, Q., Schweiger, A., L'Heureux, M., Battisti, D. S., Po-Chedley, S., Johnson, N. C., ... Steig, E. J. (2017). Influence of high-latitude atmospheric circulation changes on summertime Arctic sea ice. *Nature Climate Change*, *7*, 289-295. doi: 10.1038/nclimate3241

Docquier, D., Grist, J. P., Roberts, M. J., Roberts, C. D., Semmler, T., Ponsoni, L., … Fichefet, T. (2019). Impact of model resolution on Arctic sea ice and North Atlantic Ocean heat transport. *Climate Dynamics*, *53*, 4989–5017. doi: 10.1007/s00382-019-04840-y

Docquier, D., & Koenigk, T. (2021). Observation-based selection of climate models projects Arctic ice-free summers around 2035. *Communications Earth and Environment*, *2*(144). doi: 10.1038/s43247-021-00214-7

Docquier, D., Koenigk, T., Fuentes-Franco, R., Karami, M. P., & Ruprich-Robert, Y. (2021). Impact of ocean heat transport on the Arctic sea-ice decline: a model study with EC-Earth3. *Climate Dynamics*, *56*, 1407-1432. doi: 10.1007/s00382-020-05540-8

Eyring, V., Bony, S., Meehl, G. A., Senior, C. A., Stevens, B., Stouffer, R. J., & Taylor, K. E. (2016). Overview of the Coupled Model Intercomparison Project Phase 6 (CMIP6) experimental design and organization. *Geoscientific Model Development*, *9*, 1937-1958. doi: 10.5194/gmd-9-1937-2016

Fisher, R. A. (1992). *Statistical Methods for Research Workers. In: Breakthroughs in Statistics. Springer Series in Statistics (Perspectives in Statistics) [S. Kotz, N.L. Johnson (eds.)].* (Springer, New York) doi: 10.1007/978-1-4612-4380-96

Goosse, H., Kay, J. E., Armour, K. C., Bodas-Salcedo, A., Chepfer, H., Docquier, D., … Vancoppenolle, M. (2018). Quantifying climate feedbacks in polar regions. *Nature Communications*, *9*(1919), 1-13. doi: 10.1038/s41467-018-04173-0

Granger, C. W. (1969). Investigating causal relations by econometric models and cross-spectral methods. *Econometrica*, *37*(3), 424-438. doi: 10.2307/1912791

Harries, D., & O'Kane, T. J. (2021). Dynamic Bayesian networks for evaluation of Granger causal relationships in climate reanalyses. *Journal of Advances in Modeling Earth Systems*, *13*(5), e2020MS002442. doi: 10.1029/2020MS002442

IPCC. (2019). *Summary for Policymakers. In: IPCC Special Report on the Ocean and Cryosphere in a Changing Climate [H.-O. Pörtner, D.C. Roberts, V. Masson-Delmotte, P. Zhai, M. Tignor, E. Poloczanska, K. Mintenbeck, M. Nicolai, A. Okem, J. Petzold, B. Rama, N. Weyer (eds.)].* (Cambridge University Press, Cambridge, United Kingdom and New York, NY, USA)

Jahn, A., Kay, J. E., Holland, M. M., & Hall, D. M. (2016). How predictable is the timing of a summer ice-free Arctic? *Geophysical Research Letters*, *43*, 9113-9120. doi: 10.1002/2016GL070067

Krakovska, A., Jakubik, J., Chvostekova, M., Coufal, D., Jajcay, N., & Palus, M. (2018). Comparison of six methods for the detection of causality in a bivariate time series. *Physical Review E*, *97*(4), 042207. doi: 10.1103/PhysRevE.97.042207

Kretschmer, M., Coumou, D., Donges, J. F., & Runge, J. (2016). Using causal effect networks to analyze different Arctic drivers of midlatitude winter circulation. *Journal of Climate*, *29*(11), 4069-4081. doi: 10.1175/JCLI-D-15-0654.1

Kwok, R. (2018). Arctic sea ice thickness, volume, and multiyear ice coverage: losses and coupled variability (1958-2018). *Environmental Research Letters*, *13*(10), 105005. doi: 10.1088/1748-9326/aae3ec

Liang, X. S. (2014). Unraveling the cause-effect relation between time series. *Physical Review E*, *90*, 052150. doi: 10.1103/PhysRevE.90.052150

Liang, X. S. (2021). Normalized multivariate time series causality analysis and causal graph reconstruction. *Entropy*, *23*(6), 679. doi: 10.3390/e23060679

Liang, X. S., & Kleeman, R. (2005). Information transfer between dynamical system components. *Physical Review Letters*, *95*(24), 244101. doi: 10.1103/PhysRevLett.95.244101

Lindsay, R., & Schweiger, A. (2015). Arctic sea ice thickness loss determined using subsurface, aircraft, and satellite observations. *The Cryosphere*, *9*, 269-283. doi: 10.5194/tc-9-269-2015

Massonnet, F., Vancoppenolle, M., Goosse, H., Docquier, D., Fichefet, T., & Blanchard-Wrigglesworth, E. (2018). Arctic sea-ice change tied to its mean state through thermodynamic processes. *Nature Climate Change*, *8*, 599-603. doi: 10.1038/s41558-018-0204-z

Mosedale, T. J., Stephenson, D. B., Collins, M., & Mills, T. C. (2006). Granger causality of coupled climate processes: Ocean feedback on the North Atlantic Oscillation. *Journal of Climate*, *19*(7), 1182-1194. doi: 10.1175/JCLI3653.1

Notz, D., & Stroeve, J. (2016). Observed Arctic sea-ice loss directly follows anthropogenic CO2 emission. *Science*, *354*(6313), 747-750. doi: 10.1126/science.aag2345

Olonscheck, D., Mauritsen, T., & Notz, D. (2019). Arctic sea-ice variability is primarily driven by atmospheric temperature fluctuations. *Nature Geoscience*, *12*, 430-434. doi: 10.1038/s41561-019-0363-1

Onarheim, I. H., Eldevik, T., Arthun, M., Ingvaldsen, R. B., & Smedsrud, L. H. (2015). Skillful prediction of Barents Sea ice cover. *Geophysical Research Letters*, *42*, 5364-5371. doi: 10.1002/2015GL064359

Onarheim, I. H., Eldevik, T., Smedsrud, L. H., & Stroeve, J. C. (2018). Seasonal and regional manifestation of Arctic sea ice loss. *Journal of Climate*, *31*, 4917-4932. doi: 10.1175/JCLI-D-17-0427.1

O'Neill, B. C., Tebaldi, C., van Vuuren, D. P., Eyring, V., Friedlingstein, P., Hurtt, G., ... Sanderson, B. M. (2016). The Scenario Model Intercomparison Project (ScenarioMIP) for CMIP6. *Geoscientific Model Development*, *9*, 3461-3482. doi: 10.5194/gmd-9-3461-2016

Pithan, F., & Mauritsen, T. (2014). Arctic amplification dominated by temperature feedbacks in contemporary climate models. *Nature Geoscience*, *7*, 181-184. doi: 10.1038/NGEO2071

Polyakov, I. V., Pnyushkov, A. V., Alkire, M. B., Ashik, I. M., Baumann, T. M., Carmack, E. C., ... Yulin, A. (2017). Greater role for Atlantic inflows on sea-ice loss in the Eurasian Basin of the Arctic Ocean. *Science*, *356*(6335), 285-291. doi: 10.1126/science.aai8204

Runge, J., Bathiany, S., Bollt, E., Camps-Valls, G., Coumou, D., Deyle, E., ... Zscheischler, J. (2019). Inferring causation from time series in Earth system sciences. *Nature Communications*, *10*, 2553. doi: 10.1038/s41467-019-10105-3

Sando, A. B., Gao, Y., & Langehaug, R. (2014). Poleward ocean heat transports, sea ice processes, and Arctic sea ice variability in NorESM1-M simulations. *Journal of Geophysical Research*, *119*, 2095-2108. doi: 10.1002/2013JC009435

Schweiger, A., Wood, K. R., & Zhang, J. (2019). Arctic sea ice volume variability over 1901-2010: A model-based reconstruction. *Journal of Climate*, *32*(15), 4731-4752. doi: 10.1175/JCLI-D-19-0008.1

Serreze, M. C., Barrett, A. P., Crawford, A. D., & Woodgate, R. A. (2019). Monthly variability in Bering Strait oceanic volume and heat transports, links to atmospheric circulation and ocean temperature, and implications for sea ice conditions. *Journal of Geophysical Research*, *124*(12), 9317-9337. doi: 10.1029/2019JC015422

SIMIP Community. (2020). Arctic sea ice in CMIP6. *Geophysical Research Letters*, *47*(10), e2019GL086749. doi: 10.1029/2019GL086749

Stips, A., Macias, D., Coughlan, C., Garcia-Gorriz, E., & Liang, X. S. (2016). On the causal structure between CO2 and global temperature. *Scientific Reports*, *6*, 21691. doi: 10.1038/srep21691

Stroeve, J., & Notz, D. (2018). Changing state of Arctic sea ice across all seasons. *Environmental Research Letters*, *13*(10), 103001. doi: 10.1088/1748-9326/aade56

Sugihara, G., May, R., Ye, H., h. Hsieh, C., Deyle, E., Fogarty, M., & Munch, S. (2012). Detecting causality in complex ecosystems. *Science*, *338*(6106), 496-500. doi: 10.1126/science.1227079

Swart, N. C., Fyfe, J. C., Hawkins, E., Kay, J. E., & Jahn, A. (2015). Influence of internal variability on Arctic sea-ice trends. *Nature Climate Change*, *5*, 86-89. doi: 10.1038/nclimate2483

Tsonis, A. A., Deyle, E. R., May, R. M., Sugihara, G., Swanson, K., Verbeten, J. D., & Wang, G. (2015). Dynamical evidence for causality between galactic cosmic rays and interannual variation in global temperature. *Proceedings of the National Academy of Sciences of the United States of America*, *112*(11), 3253-3256. doi: 10.1073/pnas.1420291112

van der Linden, E. C., LeBars, D., Bintanja, R., & Hazeleger, W. (2019). Oceanic heat transport into the Arctic under high and low CO2 forcing. *Climate Dynamics*, *53*, 4763-4780. doi: 10.1007/s00382-019-04824-y

Vannitsem, S., Dalaiden, Q., & Goosse, H. (2019). Testing for dynamical dependence: Application to the surface mass balance over Antarctica. *Geophysical Research Letters*, *46*(21), 12125-12135. doi: 10.1029/2019GL084329

Vannitsem, S., & Ekelmans, P. (2018). Causal dependences between the coupled ocean–atmosphere dynamics over the tropical Pacific, the North Pacific and the North Atlantic. *Earth System Dynamics*, *9*, 1063-1083. doi: 10.5194/esd-9-1063-2018

Wunderling, N., Willeit, M., Donges, J. F., & Winkelmann, R. (2020). Global warming due to loss of large ice masses and Arctic summer sea ice. *Nature Communications*, *11*(5177). doi: 10.1038/s41467-020-18934-3

Wyser, K., Koenigk, T., Fladrich, U., Fuentes-Franco, R., Karami, M. P., & Kruschke, T. (2021). The SMHI Large Ensemble (SMHI-LENS) with EC-Earth3.3.1. *Geoscientific Model Development*, *14*, 4781-4796. doi: 10.5194/gmd-14-4781-2021

Zhang, J., Sheng, Z., Ma, Y., He, Y., Zuo, X., & He, M. (2021). Analysis of the positive Arctic Oscillation Index event and its influence in the winter and spring of 2019/2020. *Frontiers in Earth Science*, *8*(580601), 1-17. doi: 10.3389/feart.2020.580601

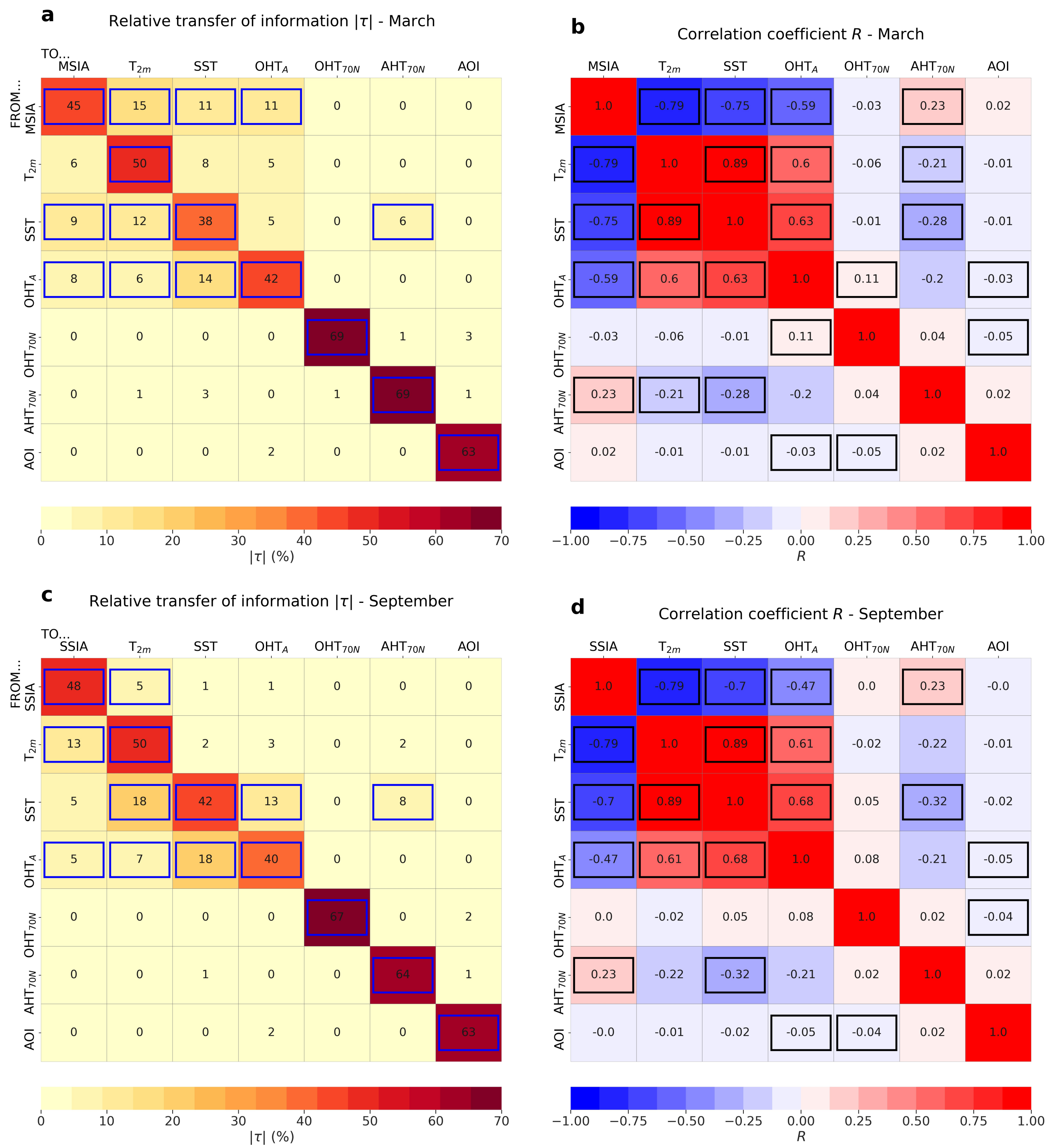

Figure 2. Matrices of EC-Earth3 ensemble mean (a,c) relative rate of information transfer τ (in absolute value; unit: %) and (b,d) correlation coefficient R between (a,b) March Arctic sea-ice area (MSIA, 1970-2080), (c,d) September sea-ice area (SSIA, 1970-2040) and the six drivers for which acronym definitions are provided in the caption of Figure 1, based on historical CMIP6 run and SSP5-8.5 scenario. The highlighted elements are significant at the 5% level based on Fisher's method for multiple tests.

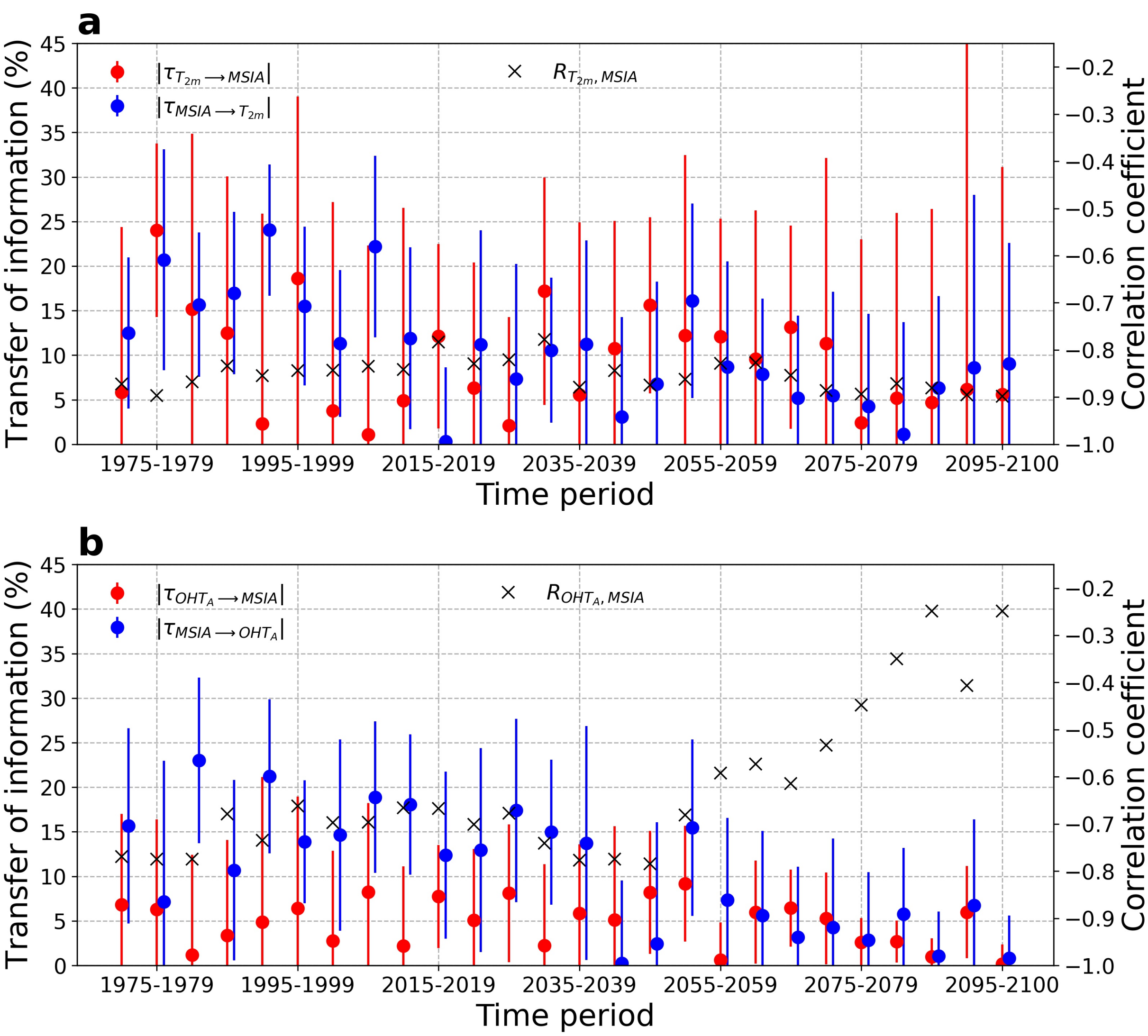

Figure 3. Time evolution of relative rate of information transfer τ (in absolute value; left axis) and correlation coefficient R (right axis) for each period of five years between 1970 and 2100 (historical CMIP6 run and SSP5-8.5 scenario), computed over the 50 EC-Earth3 members. (a) Transfer of information from annual mean Arctic near-surface air temperature (T_{2m}) to March Arctic sea-ice area (MSIA) (red circles), from MSIA to T_{2m} (blue circles), and correlation coefficient between T_{2m} and MSIA (black crosses). (b) Transfer of information from annual mean total Arctic Ocean heat transport (OHT_A) to MSIA (red circles), from MSIA to OHT_A (blue circles), and correlation coefficient between OHT_A and MSIA (black crosses). The error bars show the 95% confidence intervals for τ using bootstrap with replacement.

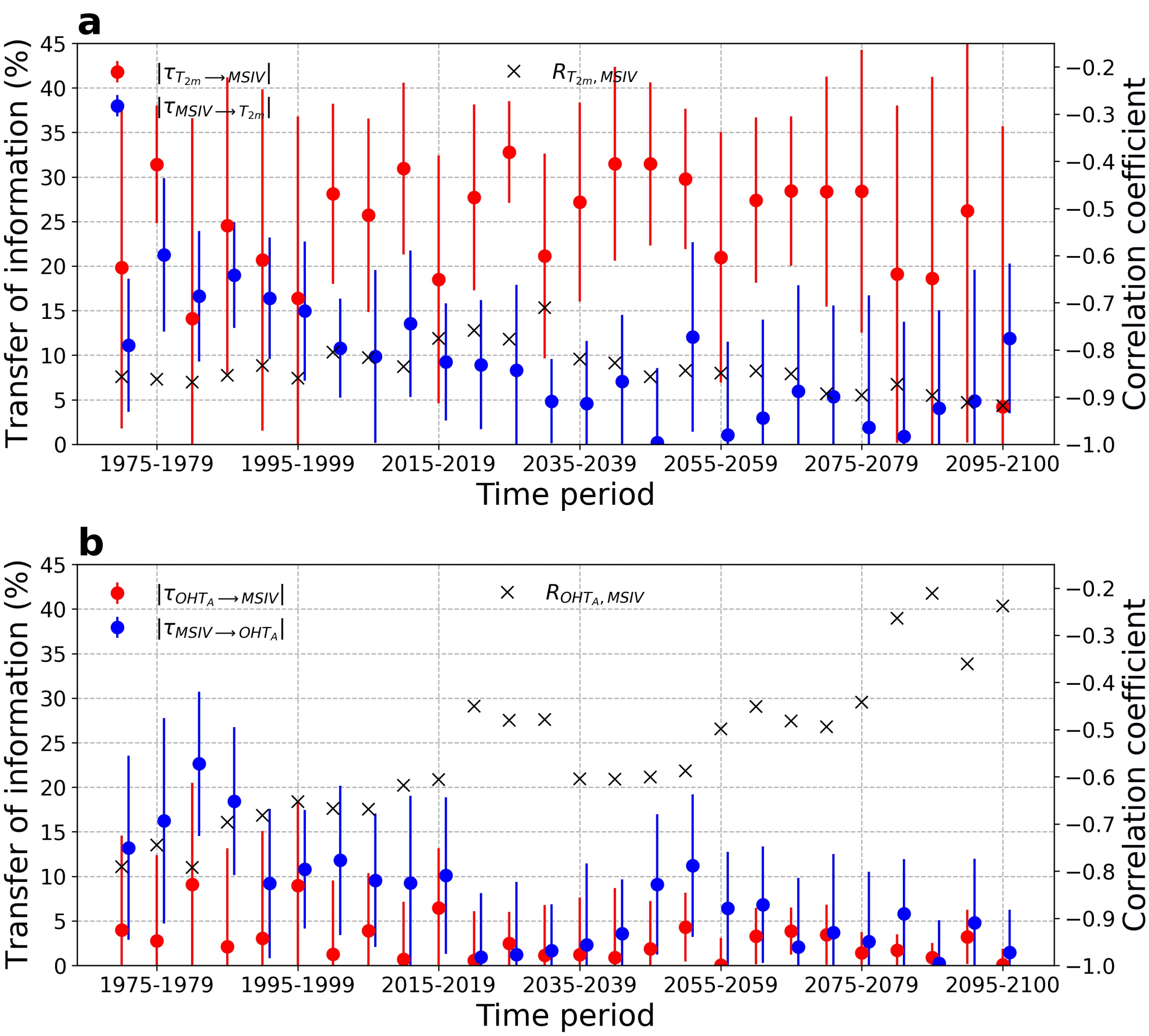

Figure 4. Time evolution of relative rate of information transfer τ (in absolute value; left axis) and correlation coefficient R (right axis) for each period of five years between 1970 and 2100 (historical CMIP6 run and SSP5-8.5 scenario), computed over the 50 EC-Earth3 members. (a) Transfer of information from annual mean Arctic near-surface air temperature (T_{2m}) to March Arctic sea-ice volume (MSIV) (red circles), from MSIV to T_{2m} (blue circles), and correlation coefficient between T_{2m} and MSIV (black crosses). (b) Transfer of information from annual mean total Arctic Ocean heat transport (OHT_A) to MSIV (red circles), from MSIV to OHT_A (blue circles), and correlation coefficient between OHT_A and MSIV (black crosses). The error bars show the 95% confidence intervals for τ using bootstrap with replacement.

Supporting Information for 'Causal links between Arctic sea ice and its potential drivers based on the rate of information transfer'

D. Docquier[1], S. Vannitsem[1], F. Ragone[1,2], K. Wyser[3], X. S. Liang[4]

[1]Royal Meteorological Institute of Belgium, Brussels, Belgium

[2]Université catholique de Louvain, Louvain-la-Neuve, Belgium

[3]Rossby Centre, Swedish Meteorological and Hydrological Institute, Norrköping, Sweden

[4]Fudan University, Shanghai, China

Contents of this file

- Introduction
- Supporting Methods
- Table S1
- Figures S1 to S11

Corresponding author: D. Docquier, Royal Meteorological Institute of Belgium, Brussels, Belgium (david.docquier@meteo.be)

Introduction

This supporting information contains additional methodological information (Supporting Methods), tables (Table S1) and figures (Figures S1-S11). Table S1 provides results of information transfer from a two-dimensional stochastic linear system of equations to check the effect of detrending data. Figure S1 shows the times series of all considered variables based on SSP1-1.9 (same as Figure 1, except for the scenario). Figure S2 shows the time series of detrended variables based on SSP5-8.5 (same as Figure 1 with ensemble mean removal). Figures S3-S5 represent matrices of ensemble mean relative rate of information transfer and correlation coefficient, similar to Figure 2, except that Figure S3 shows results from SSP1-1.9 (instead of SSP5-8.5), Figure S4 shows sea-ice volume (instead of sea-ice area), and Figure S5 shows sea-ice volume and SSP1-1.9 (instead of sea-ice area and SSP5-8.5). Figures S6-S8 represent the time evolution of the relative rate of information transfer between sea-ice area and air temperature / Arctic ocean heat transport, similar to Figure 3, except that Figure S6 shows results with September sea-ice area (instead of March sea-ice area), Figure S7 shows results from SSP1-1.9 (instead of SSP5-8.5), and Figure S8 shows results with September sea-ice area and SSP1-1.9 (instead of March sea-ice area and SSP5-8.5). Figures S9-S11 represent the time evolution of the relative rate of information transfer between sea-ice volume and air temperature / Arctic ocean heat transport, similar to Figure 4, except that Figure S9 shows results with September sea-ice volume (instead of March sea-ice volume), Figure S10 shows results from SSP1-1.9 (instead of SSP5-8.5), and Figure S11 shows results with September sea-ice volume and SSP1-1.9 (instead of March sea-ice volume and SSP5-8.5).

Supporting Methods

As explained in the main text (Section 2), the information flow method applies to stationary time series. We demonstrate this by computing the rate of information transfer $T_{2\to1}$ from variable X_2 to variable X_1 (based on equation (1) in the main text), using the two-dimensional stochastic linear system of equations from Liang (2014), to which we add a constant linear function:

$$\begin{aligned} dX_1 &= (-X_1 + 0.5\,X_2 + c\,t)\,dt + 0.1\,dW_1 \\ dX_2 &= (-X_2 + c\,t)\,dt + 0.1\,dW_2, \end{aligned} \tag{1}$$

where t is time and varies between 0 and 100 with 100,000 time steps ($\Delta t = 0.001$), c is a constant external forcing mimicking the effect of greenhouse gas emissions on temperature and sea ice, W_1 and W_2 represent normal random noises (standard Wiener process). We use eight values of c between 0 and 0.02 and compute the corresponding absolute rates of information transfer $T_{2\to1}$ and $T_{1\to2}$ for both original values of X_1 and X_2 and linearly detrended values of X_1 and X_2.

We solve the linear system (1) using the Euler-Maruyama method. Results are presented in Table S1 and show that the rates of information transfer $T_{2\to1}$ and $T_{1\to2}$ increase with c when original data are used. This suggests that the external forcing (greenhouse gas emissions in our case study) influences the value of information transfer. On the contrary, the rates of information transfer remain relatively unchanged with varying c when data are detrended, so there is no influence of the external driver on the relationship between X_1 and X_2, making results more robust.

As strong negative trends in sea-ice area and sea-ice volume and positive trends in temperature and ocean heat transport exist across the models simulations (1970-2100; Figures 1 and S1), we need to detrend data in the member analysis. As detrending based on regression strongly depends on the regression power (linear, quadratic, etc.) and we dispose of 50 different members, we choose to remove the ensemble mean from the original data in order to obtain stationary time series (Figure S2).

Table S1. Absolute rate of information transfer computed from the linear system of equations (1) with eight different values of c. $T_{2\rightarrow 1}$ and $T_{2\rightarrow 1,d}$ are the rates of information transfer from X_2 to X_1 based on original and detrended values, respectively. $T_{1\rightarrow 2}$ and $T_{1\rightarrow 2,d}$ are the rates of information transfer from X_1 to X_2 based on original and detrended values, respectively.

c	$T_{2\rightarrow 1}$	$T_{2\rightarrow 1,d}$	$T_{1\rightarrow 2}$	$T_{1\rightarrow 2,d}$
0	0.1	0.16	0.01	0.02
0.001	0.19	0.12	0.05	0.02
0.002	0.34	0.13	0.24	0.01
0.003	0.39	0.14	0.38	0.02
0.004	0.43	0.14	0.49	0.03
0.005	0.46	0.14	0.55	0.01
0.01	0.55	0.15	0.7	0.01
0.02	0.55	0.15	0.76	0.03

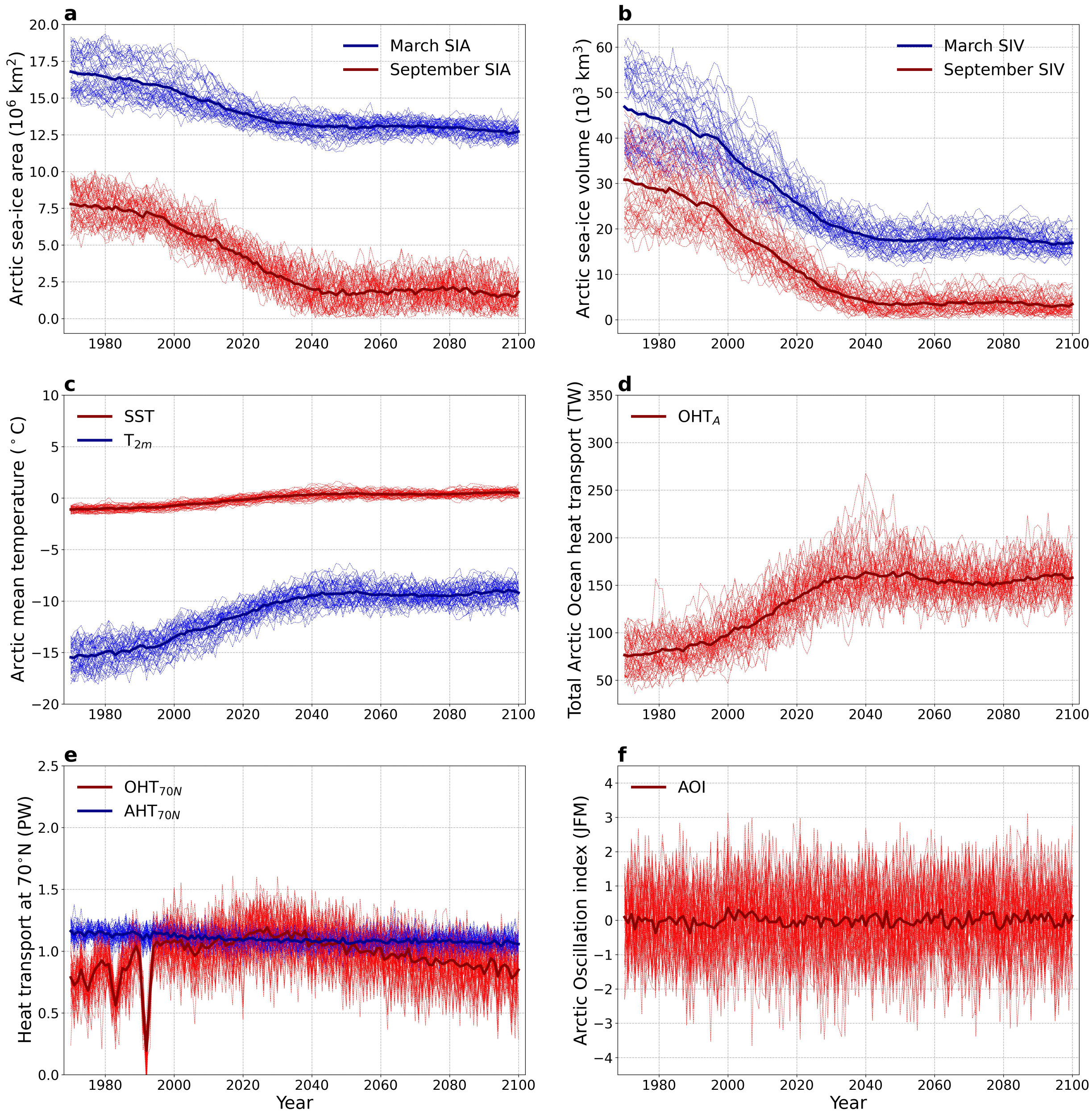

Figure S1. Time series of all considered variables for the 50 EC-Earth3 SMHI-LENS members (thin lines) and the ensemble mean (dark thick lines) over 1970-2100 (historical CMIP6 run and SSP1-1.9 scenario). (a) March and September Arctic sea-ice area (SIA); (b) March and September Arctic sea-ice volume (SIV); (c) annual mean Arctic near-surface temperature (T_{2m}) and Arctic sea-surface temperature (SST); (d) annual mean total Arctic Ocean heat transport (OHT_A); (e) annual mean poleward ocean and atmospheric heat transports at 70°N (OHT_{70N} and AHT_{70N}); (f) winter (JFM) Arctic Oscillation index (AOI).

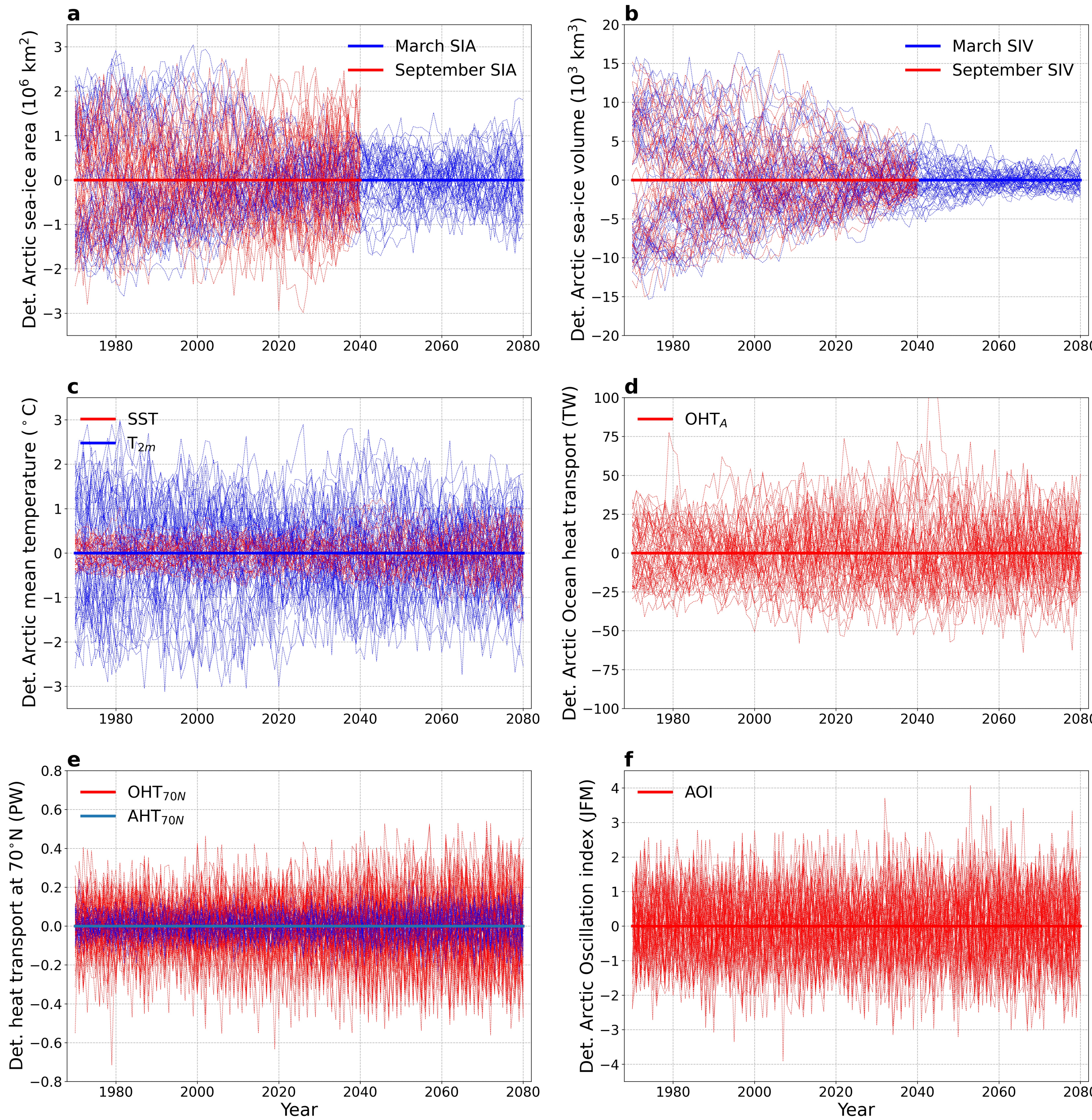

Figure S2. Time series of all considered detrended variables (same as Fig. 1 with ensemble mean removal) for the 50 EC-Earth3 SMHI-LENS members (thin lines) and the ensemble mean (dark thick lines) over 1970-2080 (historical CMIP6 run and SSP5-8.5 scenario; 1970-2040 for September sea-ice area and volume). (a) March and September Arctic sea-ice area (SIA); (b) March and September Arctic sea-ice volume (SIV); (c) annual mean Arctic near-surface temperature (T_{2m}) and Arctic sea-surface temperature (SST); (d) annual mean total Arctic Ocean heat transport (OHT_A); (e) annual mean poleward ocean and atmospheric heat transports at 70°N (OHT_{70N} and AHT_{70N}); (f) winter (JFM) Arctic Oscillation index (AOI).

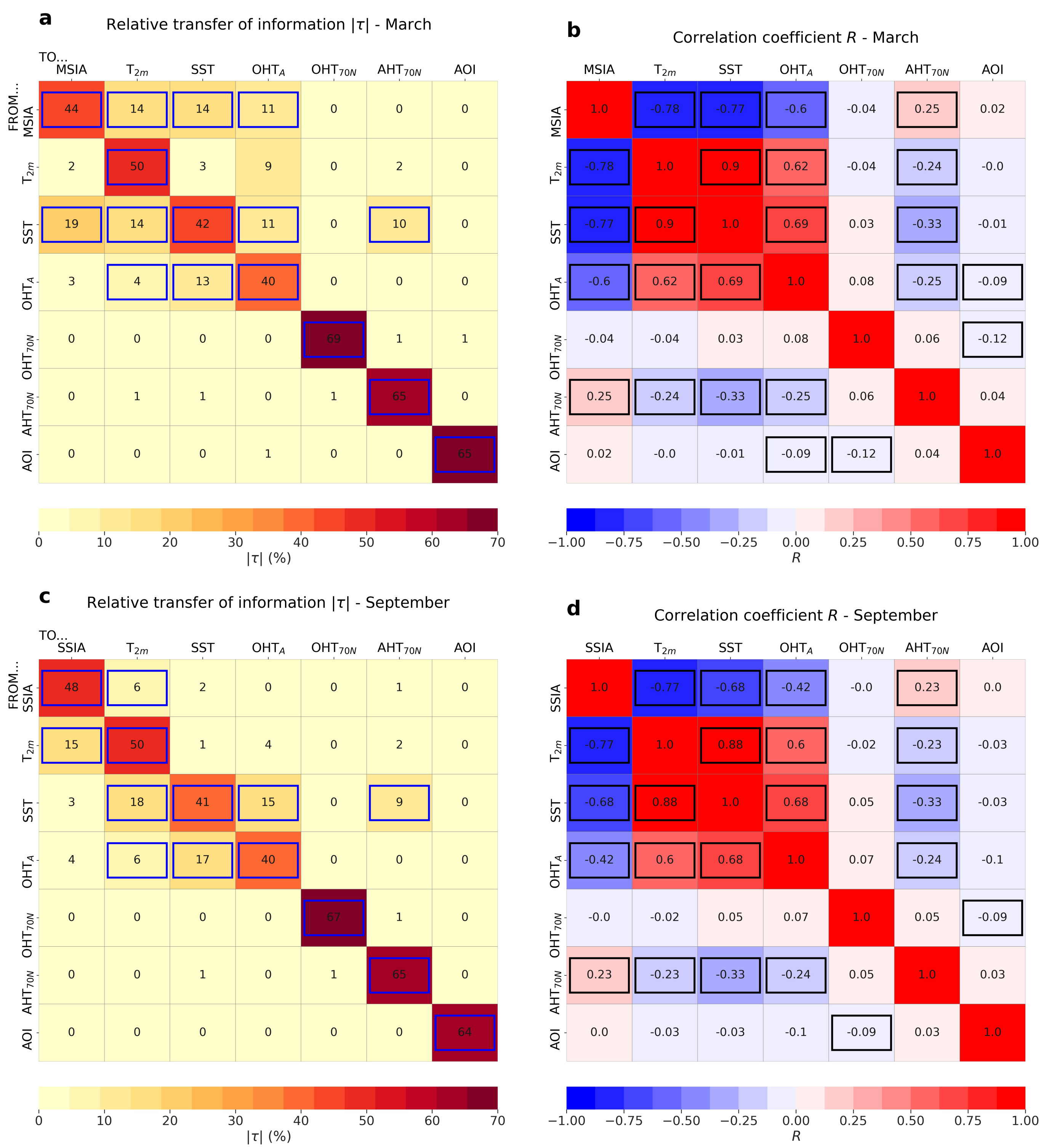

Figure S3. Matrices of EC-Earth3 ensemble mean (a,c) relative transfer of information τ (in absolute value; unit: %) and (b,d) correlation coefficient R between (a,b) March Arctic sea-ice area (MSIA, 1970-2080), (c,d) September sea-ice area (SSIA, 1970-2040) and the six drivers for which acronym definitions are provided in the caption of Figure S1, based on historical CMIP6 run and SSP1-1.9 scenario. The highlighted elements are significant at the 5% level based on Fisher's method for multiple tests.

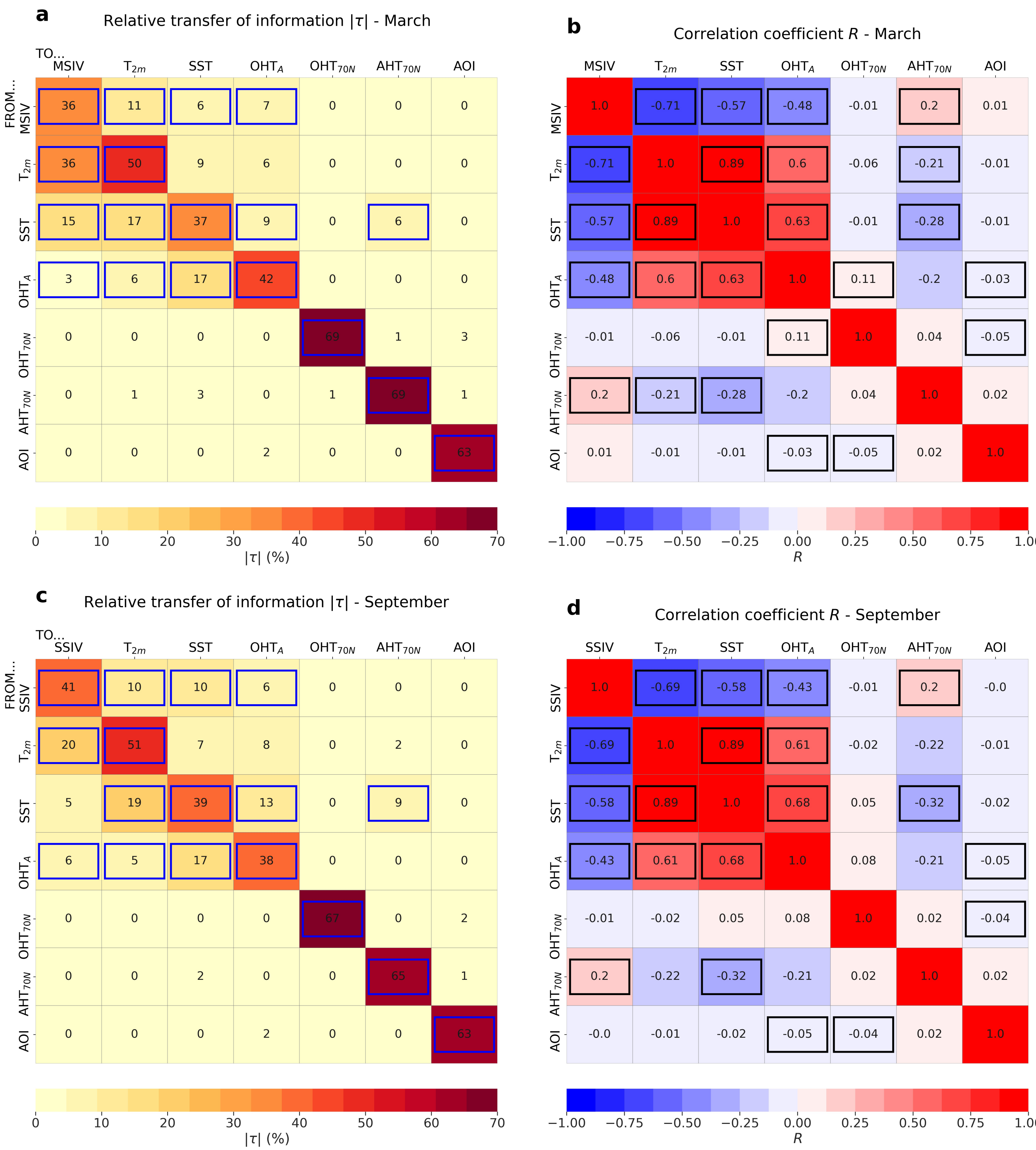

Figure S4. Matrices of EC-Earth3 ensemble mean (a,c) relative rate of information transfer τ (in absolute value; unit: %) and (b,d) correlation coefficient R between (a,b) March Arctic sea-ice volume (MSIV, 1970-2080), (c,d) September sea-ice volume (SSIV, 1970-2040) and the six drivers for which acronym definitions are provided in the caption of Figure S1, based on historical CMIP6 run and SSP5-8.5 scenario. The highlighted elements are significant at the 5% level based on Fisher's method for multiple tests.

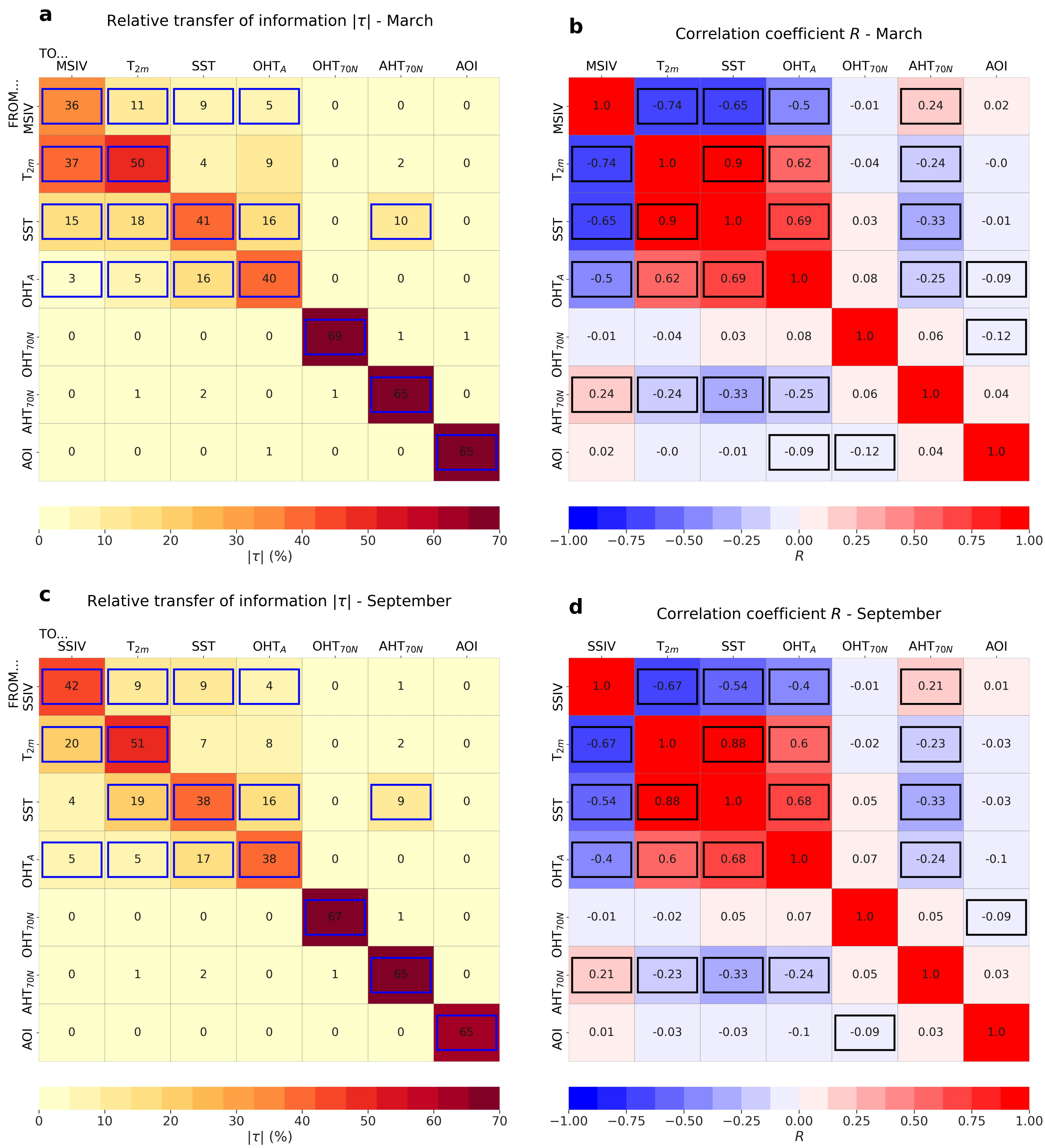

Figure S5. Matrices of EC-Earth3 ensemble mean (a,c) relative rate of information transfer τ (in absolute value; unit: %) and (b,d) correlation coefficient R between (a,b) March Arctic sea-ice volume (MSIV, 1970-2080), (c,d) September sea-ice volume (SSIV, 1970-2040) and the six drivers for which acronym definitions are provided in the caption of Figure S1, based on historical CMIP6 run and SSP1-1.9 scenario. The highlighted elements are significant at the 5% level based on Fisher's method for multiple tests.

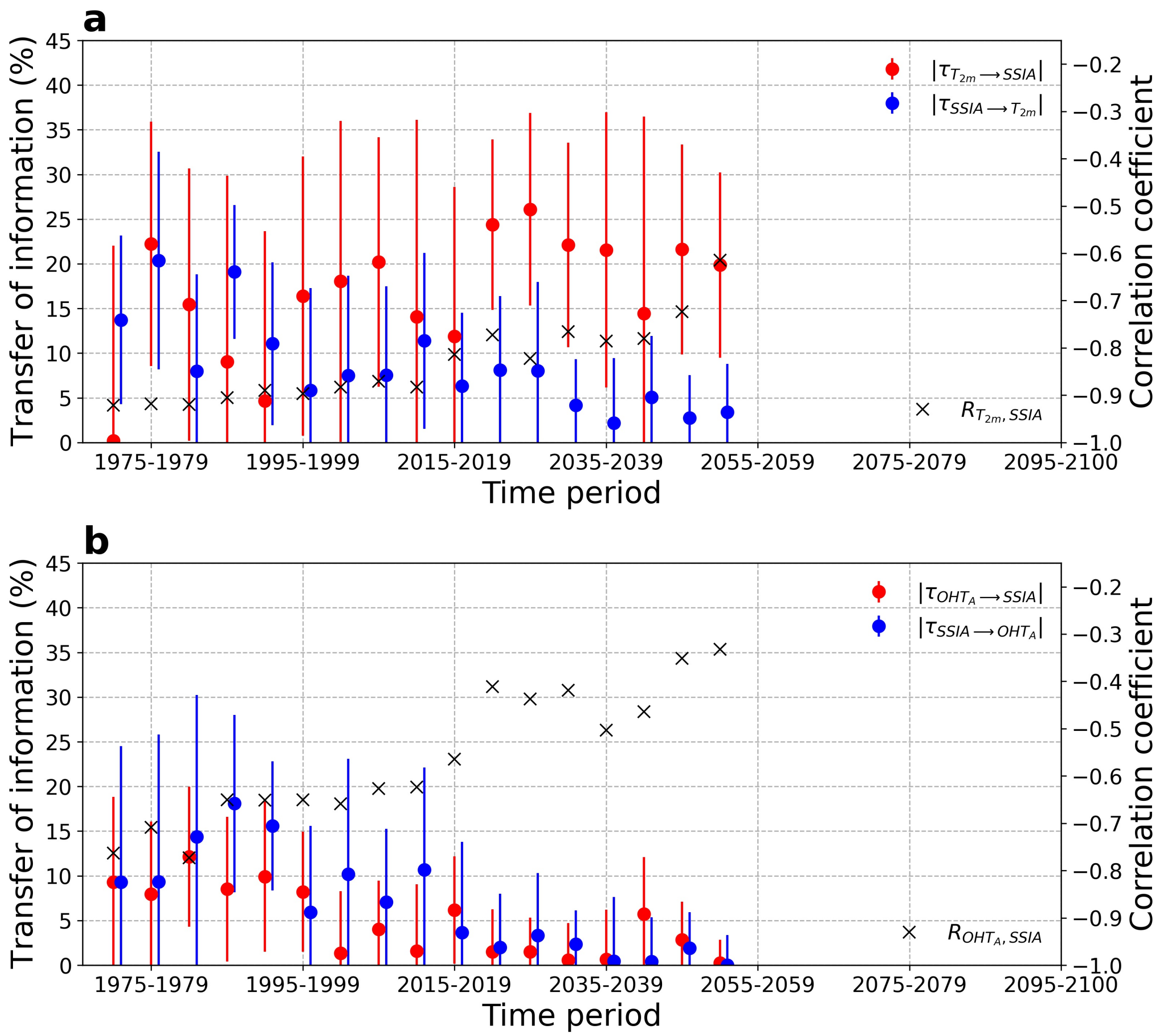

Figure S6. Time evolution of relative rate of information transfer τ (in absolute value; left axis) and correlation coefficient R (right axis) for each period of five years between 1970 and 2100 (historical CMIP6 run and SSP5-8.5 scenario), computed over the 50 EC-Earth3 members. (a) Transfer of information from annual mean Arctic near-surface air temperature (T_{2m}) to September Arctic sea-ice area (SSIA) (red circles), from SSIA to T_{2m} (blue circles), and correlation coefficient between T_{2m} and SSIA (black crosses). (b) Transfer of information from annual mean total Arctic Ocean heat transport (OHT_A) to SSIA (red circles), from SSIA to OHT_A (blue circles), and correlation coefficient between OHT_A and SSIA (black crosses). The error bars show the 95% confidence intervals for τ using bootstrap with replacement.

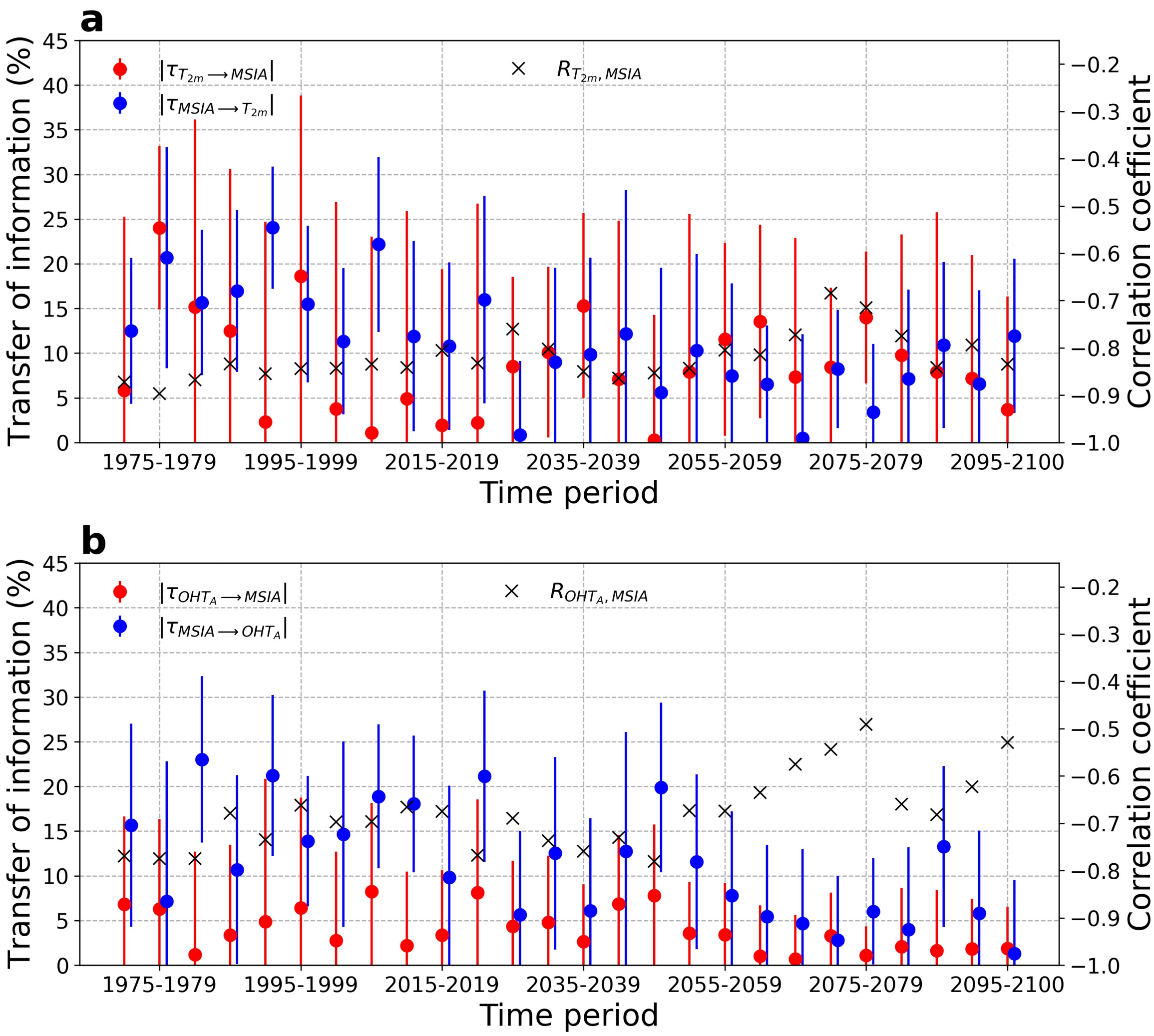

Figure S7. Time evolution of relative rate of information transfer τ (in absolute value; left axis) and correlation coefficient R (right axis) for each period of five years between 1970 and 2100 (historical CMIP6 run and SSP1-1.9 scenario), computed over the 50 EC-Earth3 members. (a) Transfer of information from annual mean Arctic near-surface air temperature (T_{2m}) to March Arctic sea-ice area (MSIA) (red circles), from MSIA to T_{2m} (blue circles), and correlation coefficient between T_{2m} and MSIA (black crosses). (b) Transfer of information from annual mean total Arctic Ocean heat transport (OHT_A) to MSIA (red circles), from MSIA to OHT_A (blue circles), and correlation coefficient between OHT_A and MSIA (black crosses). The error bars show the 95% confidence intervals for τ using bootstrap with replacement.

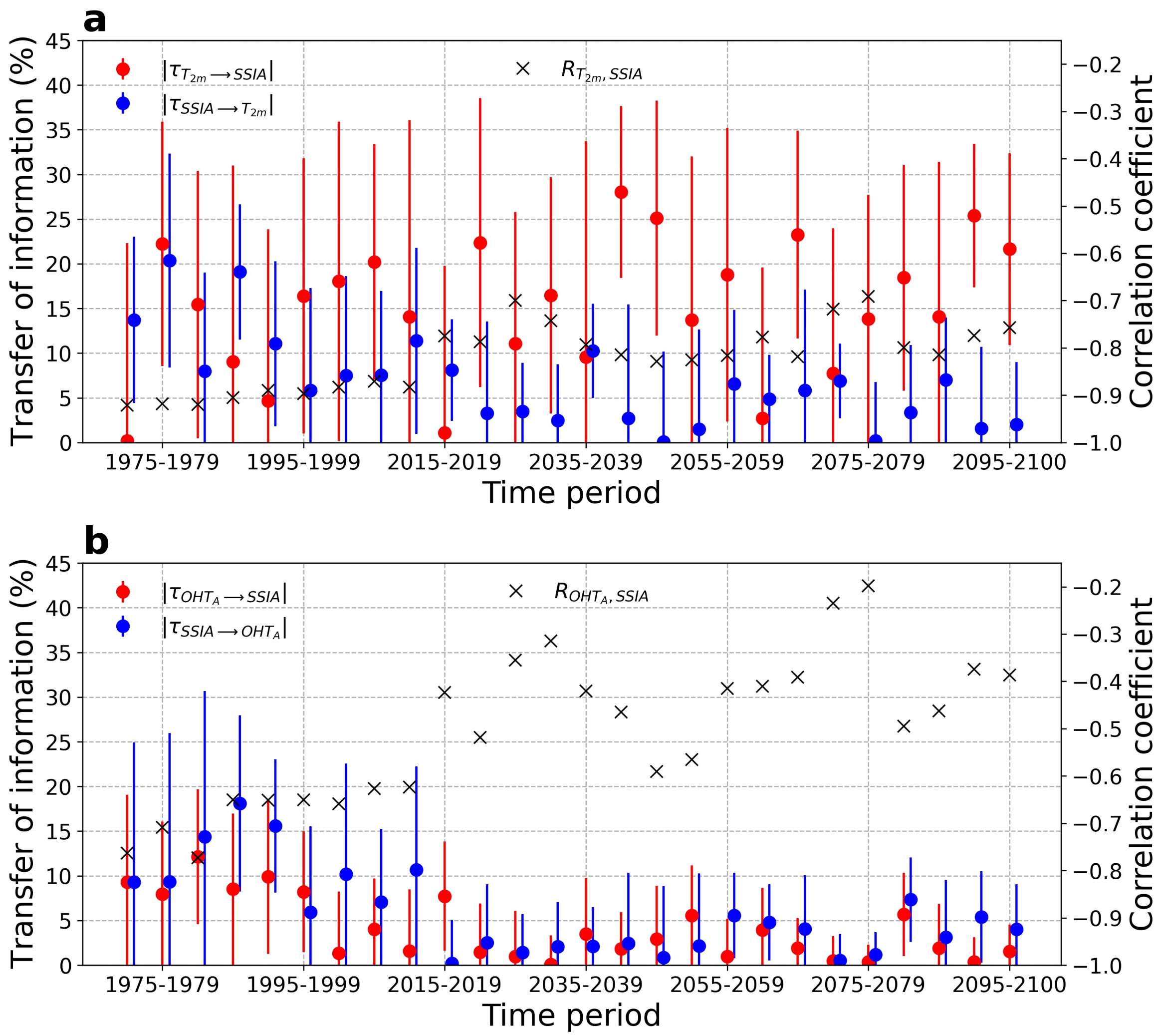

Figure S8. Time evolution of relative rate of information transfer τ (in absolute value; left axis) and correlation coefficient R (right axis) for each period of five years between 1970 and 2100 (historical CMIP6 run and SSP1-1.9 scenario), computed over the 50 EC-Earth3 members. (a) Transfer of information from annual mean Arctic near-surface air temperature (T_{2m}) to September Arctic sea-ice area (SSIA) (red circles), from SSIA to T_{2m} (blue circles), and correlation coefficient between T_{2m} and SSIA (black crosses). (b) Transfer of information from annual mean total Arctic Ocean heat transport (OHT_A) to SSIA (red circles), from SSIA to OHT_A (blue circles), and correlation coefficient between OHT_A and SSIA (black crosses). The error bars show the 95% confidence intervals for τ using bootstrap with replacement.

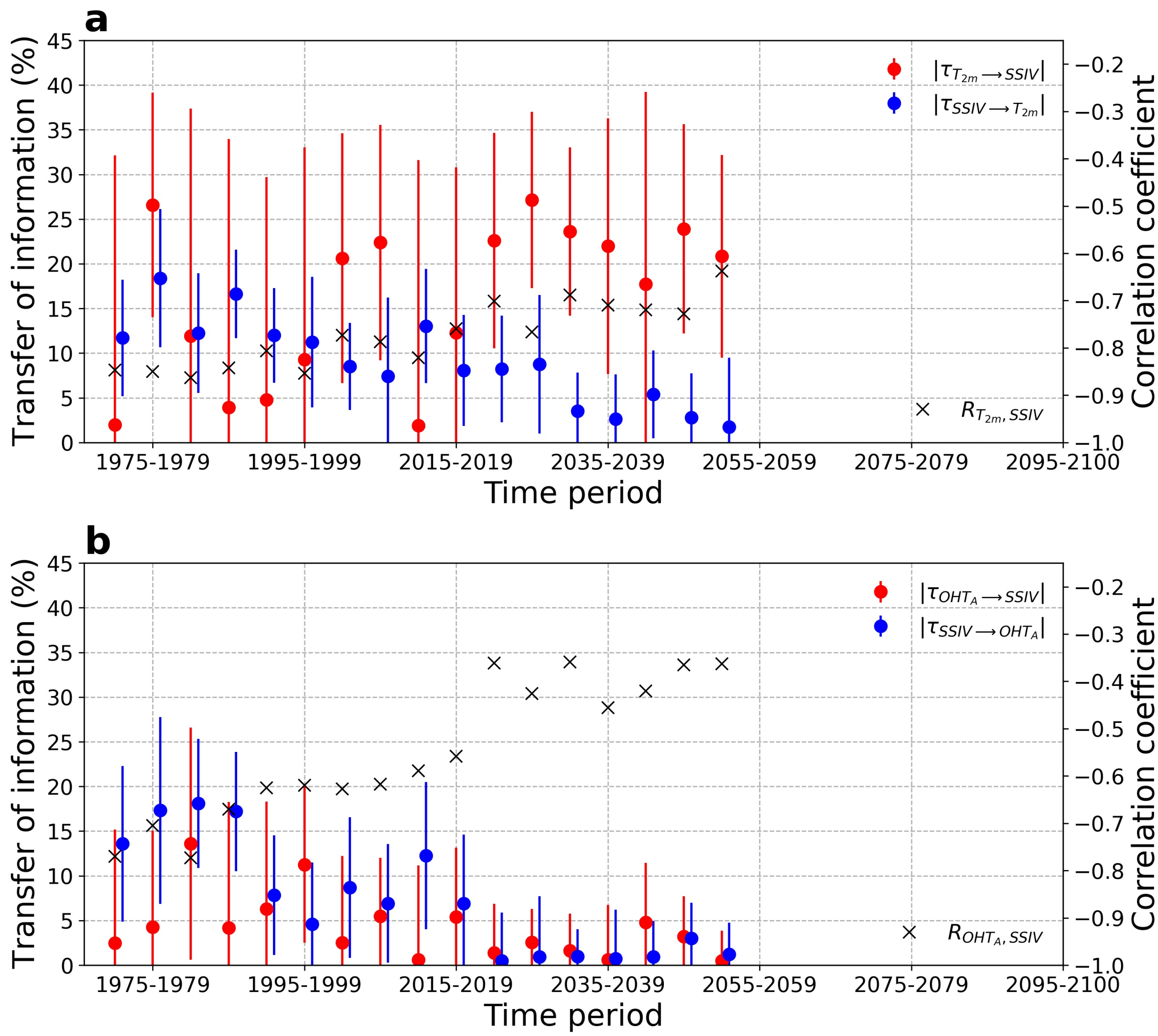

Figure S9. Time evolution of relative rate of information transfer τ (in absolute value; left axis) and correlation coefficient R (right axis) for each period of five years between 1970 and 2100 (historical CMIP6 run and SSP5-8.5 scenario), computed over the 50 EC-Earth3 members. (a) Transfer of information from annual mean Arctic near-surface air temperature (T_{2m}) to September Arctic sea-ice volume (SSIV) (red circles), from SSIV to T_{2m} (blue circles), and correlation coefficient between T_{2m} and SSIV (black crosses). (b) Transfer of information from annual mean total Arctic Ocean heat transport (OHT_A) to SSIV (red circles), from SSIV to OHT_A (blue circles), and correlation coefficient between OHT_A and SSIV (black crosses). The error bars show the 95% confidence intervals for τ using bootstrap with replacement.

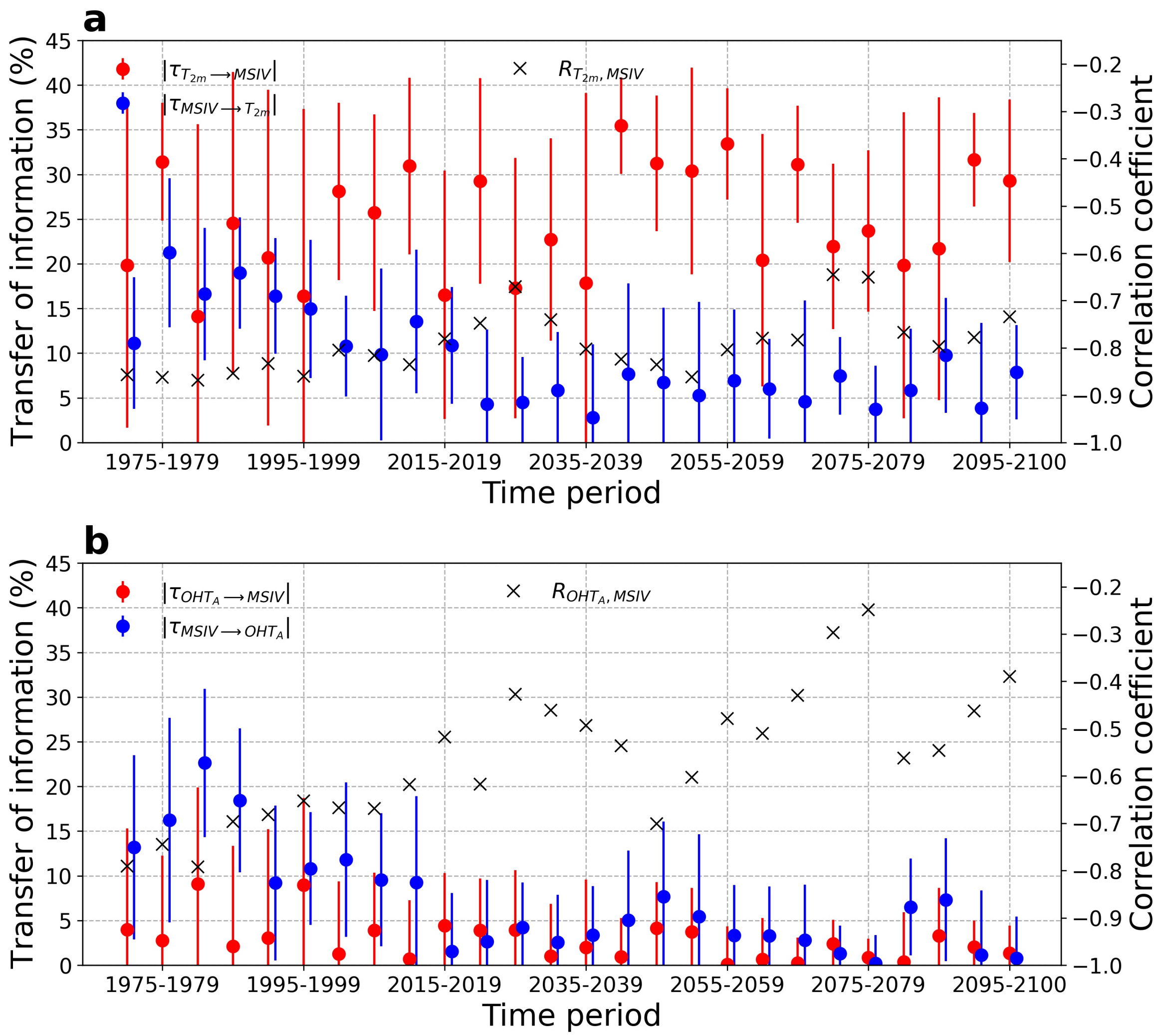

Figure S10. Time evolution of relative rate of information transfer τ (in absolute value; left axis) and correlation coefficient R (right axis) for each period of five years between 1970 and 2100 (historical CMIP6 run and SSP1-1.9 scenario), computed over the 50 EC-Earth3 members. (a) Transfer of information from annual mean Arctic near-surface air temperature (T_{2m}) to March Arctic sea-ice volume (MSIV) (red circles), from MSIV to T_{2m} (blue circles), and correlation coefficient between T_{2m} and MSIV (black crosses). (b) Transfer of information from annual mean total Arctic Ocean heat transport (OHT_A) to MSIV (red circles), from MSIV to OHT_A (blue circles), and correlation coefficient between OHT_A and MSIV (black crosses). The error bars show the 95% confidence intervals for τ using bootstrap with replacement.

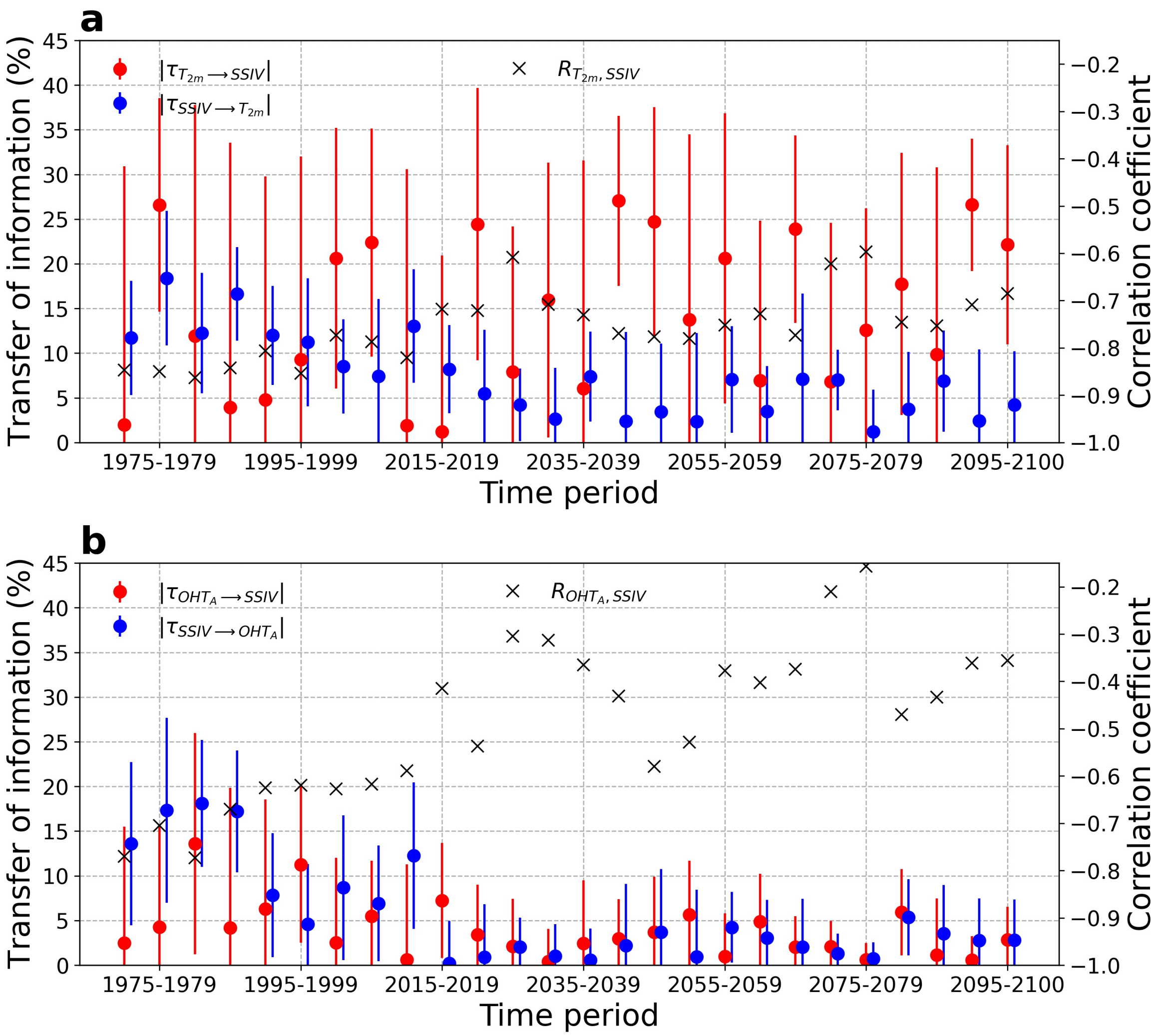

Figure S11. Time evolution of relative rate of information transfer τ (in absolute value; left axis) and correlation coefficient R (right axis) for each period of five years between 1970 and 2100 (historical CMIP6 run and SSP1-1.9 scenario), computed over the 50 EC-Earth3 members. (a) Transfer of information from annual mean Arctic near-surface air temperature (T_{2m}) to September Arctic sea-ice volume (SSIV) (red circles), from SSIV to T_{2m} (blue circles), and correlation coefficient between T_{2m} and SSIV (black crosses). (b) Transfer of information from annual mean total Arctic Ocean heat transport (OHT_A) to SSIV (red circles), from SSIV to OHT_A (blue circles), and correlation coefficient between OHT_A and SSIV (black crosses). The error bars show the 95% confidence intervals for τ using bootstrap with replacement.